Modeling and Simulation of Multilayer MoS_2 Schottky Barrier Field-Effect Transistors

by

Zhuoyang He

A thesis
presented to the University of Waterloo
in fulfillment of the
thesis requirement for the degree of
Master of Applied Science
in
Electrical and Computer Engineering

Waterloo, Ontario, Canada, 2024

© Zhuoyang He 2024

Author's Declaration

I hereby declare that I am the sole author of this thesis. This is a true copy of the thesis, including any required final revisions, as accepted by my examiners.

I understand that my thesis may be made electronically available to the public.

Abstract

As a member of the transition metal dichalcogenide (TMDCs) family, Molybdenum Disulfide (MoS_2) exhibits a layered 2D structure with exceptional electronic and optoelectronic properties, making MoS_2 a promising candidate for next-generation nano-devices. However, despite numerous efforts in synthesis, fabrication process, and device structure for few-layer MoS_2. A key challenge that remains is the Fermi-pinning effect. Due to defects distributed at the MoS_2/metal interface, the Schottky-mott rule fails to predict the Schottky barrier height based on the Fermi-level difference between MoS_2 and the metal. Instead, the Fermi level of the metal is pinned near the conduction band edge regardless of the work function of the metal used. This phenomenon results in an inevitable Schottky barrier, which must be recognized in device simulations.

In this thesis, the electrical and optoelectronic performance of multilayer MoS_2 field-effect transistors is predicted and analyzed through simulation techniques. Drift-diffusion equations are employed to model electronic properties, utilizing finite element methods (FEM) to solve the corresponding partial differential equations. FEM discretizes space and divides the solution domain into finite elements. For optoelectronic simulations, When solving Maxwell's equation for optical absorption and carrier generation rates. Finite-Difference Time Domain (FDTD) methods are applied, which discretize both space and time, representing fields as discrete values on a grid in both dimensions.

We aim to examine the effect of Schottky barrier height on MoS2-based devices and complete the missing p-branch of MoS_2 SBFETs due to the Fermi-pinning effect. Initially, we verify our model against experimental data, results prove the capability of our model to predict the electrical performance of Schottky barrier FETs. By varying the Schottky barrier height from 0 eV to 1.3 eV across the MoS_2 bandgap, a transition from n-type transport to p-type transport is observed. However, the ambipolar transport is limited by the relatively large bandgap. Ambipolarity is enabled through asymmetric metal configurations, as evidenced by simulations showing that the Pd-Au configuration can achieve ambipolar behavior with currents comparable to symmetric MoS_2-based FETs.

Furthermore, we simulate dual-gated FETs by incorporating an additional gate, allowing for reconfigurability between NP and PN configurations. These devices exhibit an outstanding rectification ratio that can be optimized under low gate voltage conditions. Nevertheless, the asymmetry in performance between PN and NP configurations indicates the significant impact of metal choices. The successful establishment of $p - n$ junction in the dual-gated devices illustrates their potential as photodetectors. Simulation results indicate a photoresponsivity of 24.2 mA/W for PN configuration, this relatively low photoresponsivity should be attributed to the existence of the Schottky barrier and multilayer

MoS_2's direct band gap. Furthermore, a deeper investigation studies the respective contribution to the photocurrent of $p-n$ junction and the Schottky junction. The results show that the $p-n$ junction suppresses the current originating from the Schottky barrier. Therefore, once a $p-n$ junction is created with gating voltages, it consistently remains the main contributor to the photocurrent and the maximum photocurrent is optimized at a gating voltage of 2 V.

Acknowledgements

I would like to express my sincere gratitude to several people who made this thesis possible.

First of all, I would like to thank my supervisor Prof. Na Young Kim, for her continuous support, guidance, and encouragement. Her expertise and insightful feedback played a vital role in the completion of this work. Moreover, her rigorous and meticulous approach to scientific research has had a profound impact on my future personal development.

I am also grateful to the readers of this thesis, Prof. Michael Pope, and William Wong, for their reviews and suggestions, which greatly improved the quality of this thesis.

I would like to thank my lab mates, Heebong Yang, and Bowen Deng, for their valuable suggestions for research and friendship.

Special thanks go to my friend, Ruofei Zheng, for her companionship and support throughout my Master's journey.

Lastly, I extend my appreciation to my family, my parents, grandparents, and my two little sisters, for their love in all direct or indirect forms. Without you, I would not be who I am today. I love you all.

Table of Contents

Author's Declaration **ii**

Abstract **iii**

Acknowledgements **v**

List of Figures **viii**

List of Tables **xii**

1 Introduction **1**

1.1 History of 2D Materials 1

1.2 Structure and Properties of MoS_2 2

1.3 MoS_2 Field-Effect Transistors 5

1.4 MoS_2 Photodetectors 8

1.5 Fermi-Pinning Effect 9

1.6 Outline of the Thesis 12

2 Theoretical background **14**

2.1 Drift-Diffusion Model 14

2.2 Metal Contacts 16

2.2.1 Thermionic Emission Model 17

2.2.2 Wentzel-Kramers-Brillouin Tunneling Model 18
2.3 Maxwell's Equations and Light Absorption 19
2.4 Simulation Scheme 20
2.4.1 Electrical Simulation 20
2.4.2 Optoelectronic simulation 23

3 Contact-Dependent Electrical Performance Simulation of Multilayer MoS_2 Transistors 25
3.1 Modeling Setup and Parameters 25
3.2 Model Verification 27
3.3 Tunneling Currents in MoS_2 SBFETs 29
3.4 Contact Area-Dependent Electron Transport in MoS_2 SBFETs 31
3.5 MoS_2 SBFETs with Schottky Barrier Height across Bandgap 33
3.6 Ambipolar MoS_2 SBFETs with Asymmetric Electrode Metals 36

4 Electrical and Optical Performance Simulation of Dual-gated MoS_2 FETs 40
4.1 Modeling Setup and Parameter 40
4.2 Electrical Performance Simulation of Dual-gated MoS_2 FETs 42
4.2.1 Reconfigurable Functionality through Gate Voltage Control 42
4.2.2 Study of Diode Behavior in PN Configuration 44
4.3 Optoelectronic Performance Simulation of Dual-gated MoS_2 FETs 47
4.3.1 Model Setup and Parameters 47
4.3.2 Device Optoelectronic Characteristics 48

5 Conclusion and prospects 51
5.1 Conclusion 51
5.2 Prospects 52

Bibliography 53

List of Figures

Figure 1.1 Crystal structures of MoS_2: (a) Top view of MoS_2 monolayer hexagonal crystal structure. (b) Trigonal prismatic (2H) and octahedral (1T) unit cell structures [19]. 3

Figure 1.2 Calculated band structures of (a) bulk MoS_2, (b) quadrilayer MoS_2, (c) bilayer MoS_2, and (d) monolayer MoS_2. The solid arrows indicate the lowest energy transitions. Bulk MoS_2 is characterized by an indirect bandgap. The direct excitonic transitions occur at high energies at K point. With reduced layer thickness, the indirect bandgap becomes larger, while the direct excitonic transition barely changes. For monolayer MoS_2 in d, it becomes a direct bandgap semiconductor. This dramatic change of electronic structure in monolayer MoS_2 can explain the observed jump in monolayer photoluminescence efficiency.[20] 4

Figure 1.3 Device structure of a (a) back-gated MoS_2 FET, (b) top-gated MoS_2 FET, (c) double-gated MoS_2 FET [6]. 6

Figure 1.4 The device structure of a (a) Photoconductor, (b) Phototransistor, (c) Photodiode [57]. 9

Figure 1.5 Energy diagrams of a p-type Ohmic contact (a), n-type Ohmic contact (b). (c) Schematic I-V characteristics of Ohmic contact. (d) Energy diagrams of a Schottky contact, for Schottky contact, it's n-type if $\Phi_{B,n} < \Phi_{B,p}$, it's p-type if $\Phi_{B,p} < \Phi_{B,n}$. Schematic I-V characteristics of single Schottky contact (e) and double Schottky contacts (f). 10

Figure 1.6 (a) Energy diagrams of Sc (Φ_{Sc} = 3.5 eV) and Pd (Φ_{Pd} = 5.1 eV) and a multilayer MoS_2 with electron affinity χ_{MoS_2} = 4.0 eV and a bandgap energy of $E_g = E_c$–E_v = 1.3 eV, where E_c and E_v are conduction band energy and valence band energy before contact. Diagrams of band alignment when Pd (blue) and Sc (red) metal contacts to multilayer MoS_2 without (b) and with (c) Fermi level pinning effect after contact. 11

Figure 2.1 The schematic of an ideal Schottky barrier and three conduction mechanisms (TE: thermionic emission, TFE: thermionic-field emission, FE: field emission) by which an electron can pass across the barrier. 17

Figure 2.2 (a) Mesh points for the FDM grid (b) Computational molecule for the 5-point star [77]. 22

Figure 2.3 FDTD Yee Cell [80]. 23

Figure 3.1 Schematic representation of the a) MoS_2-based FET device (not to scale) b) MoS_2-based FET device after meshing in COMSOL Multiphysics. 26

Figure 3.2 Comparison study of a multilayer MoS_2 SBFET simulation (solid lines) and experimental results (markers) with four metals (Sc, Ti, Ni, and Pt) reported from Ref. [66]. (a) Output characteristic of I_{DS} - V_{DS} for V_{GS} = 3 V. (b) Transconductance comparison of the I_{DS} - V_{GS} characteristic given V_{DS} = 0.2 V (b). 27

Figure 3.3 Comparison study of a multilayer MoS_2 SBFET simulation (solid lines) and experimental results (markers) with four metals (Sc, Ti, Ni, and Pt) reported from Ref. [66]. Schottky barrier height (Φ_B) as a function of applied V_{GS} for the Ni contact device, with a simulated V_{FB} of -0.5 V. . . . 29

Figure 3.4 (a) Comparison between the simulation results with and without tunneling current contribution as a function of V_{GS}, V_{DS} = 0.2 V. The corresponding band diagram at different V_{GS} from (a). (b) V_{GS}: -10 V to -1.1 V. (c) V_{GS}: -1.1 V to 10 V. 30

Figure 3.5 Thickness-dependent output characteristics of MoS_2 FETs with Ohmic contacts (a), Schottky contacts (b), V_{GS} = 0 V, $\Phi_{B,n}$ = 0.3 eV. Current density J versus different thickness of MoS_2 at V_{DS} = 0.2 V, Ohmic contacts case (c), Schottky contacts case (d). Electron density distribution near the metal/MoS_2 contacts, Ohmic contacts case (e), Schottky contacts case (f), V_{DS} = 0.2 V. 32

Figure 3.6 Quasi-Fermi level positions as a function of applied gate voltages for metal contact with different Φ_m, quasi-electron for Φ_m of 4.0 - 4.6 eV, and quasi-hole for Φ_m of 4.8 - 5.3 eV. 34

Figure 3.7 The effect of various metal contacts with a wide range of Φ_m on multilayer MoS_2 SBFETs. Transfer characteristics of *p*-type FETs (a) or *n*-type FETs (b) for metals with different Φ_m at $V_{DS} = 0.2$ V. (c) I_{DS} as a function of Φ_m of applied contact metals at different V_{GS}. (d) On/off ratio as a function of Φ_m of applied contact metals. 35

Figure 3.8 Multilayer MoS_2 SBFETs with asymmetric metal electrodes of Au (source) and Pd (drain). (a) Transfer characteristic for MoS_2 SBFETs with asymmetric metals and with symmetric metals, which are biased at V_{DS} = 1 V. (b) Corresponding energy band diagrams of MoS_2 SBFETs with asymmetric metals from (a) at $V_{GS} = \pm 10$ V. 37

Figure 3.9 Multilayer MoS_2 SBFETs with asymmetric metal electrodes of Au (source) and Pd (drain). (a) Output characteristics for MoS_2 SBFETs with asymmetric metals and with symmetric metals at $V_{GS} = \pm 3$ V. (b) Energy band diagrams of MoS_2 SBFETs with asymmetric metals from (a) at V_{DS} = 1 V (top) and -1 V (bottom) under the same $V_{GS} = 3$ V. 38

Figure 4.1 Dual-gated MoS_2 SBFETs with asymmetric electrode metals (a) Illustration of the dual-gate MoS_2 SBFET device with control gate (CG) and program gate (PG) at the bottom (b) $I_{DS} - V_{DS}$ curves showing transport characteristics of four various configurations of the device: NN, PP, PN and NP. Both gate voltages are set to be 3 V for NN and –3 V for PP. $V_{CG} = 3$ V for NP and -3 V for PN. (c) Semi-logarithmic plots of $I_{DS} - V_{DS}$ for PN configuration, with fits in red. The fits give a diode ideality factor η of 1.7 and series resistance R_s of 8 BΩ (d) Semi-logarithmic plots of $I_{DS} - V_{DS}$ for NP configuration, with fits in orange. The fits give a diode ideality factor η of 1.8 and series resistance R_s of 100 TΩ. 43

Figure 4.2 Gate voltage V_{CG} dependence of transport properties in dual-gated MoS_2 SBFETs. (a) Linear scale plot of $I_{DS} - V_{DS}$ characteristics of the $p-n$ MoS_2 dual-gate SBFET at three different V_{GS} values. Particularly, the opposite bias is applied to the CG and PG gates in $V_{CG} = -V_{PG} = V_{GS}$. (b) Logarithmic scale pot of the $I_{DS} - V_{DS}$. (c) Conduction band (E_c) profile across the $p - n$ junction region at various V_{GS} and V_{DS} = 0 V, E_c at p-type MoS_2 body (region far from the junction) is positioned at 0 eV. Barrier potential (Φ_p) is labeled as the distance between the E_c of p-type and n-type MoS_2. (d) Rectification ratio of dual-gated MoS_2 SBFETs as a function of V_{GS}. 45

Figure 4.3 Band diagrams of the negative V_{DS} (a) and the positive V_{DS} (b) to explain the rectifying behavior. 46

Figure 4.4 Schematic diagram of the FDTD(a) and CHARGE(b) model of a dual-gated MoS_2 FETs model. Real part(c) and imaginary part(d) of the dielectric function of multilayer MoS_2 in the visible region. 47

Figure 4.5 Optoelectronic behavior of dual-gated MoS_2 SBFETs. (a) Comparison of I_{DS} - V_{DS} under dark and light conditions with various incident optical power densities (λ = 532 nm, P_{inc} = 0.01, 0.1, 1, 5 mW/cm^2). (b) Responsivity as a function of incident power in logarithmic scale. 48

Figure 4.6 (a) Schematic diagrams of simulated devices in Lumerical CHARGE, showing two assumptions for the photogenerated region: entire channel material between Drain and Source (top, purple) and Schottky junction near Drain and Source (bottom, purple). (b) Overall Photocurrent (blue) and Schottky junction Photocurrent (red) as a function of different V_{GS}. (c) Band diagrams illustrating the behavior of the photogenerated carriers at different positions and conditions, top: metal contact and V_{GS} = 0 V, middle: metal contact and V_{GS} = 1 V, $p - n$ junction and V_{GS} = 1 V. 49

List of Tables

Table 1.1 Comparison of semiconductor properties between monolayer MoS_2 and multilayer MoS_2. [21, 26, 27] 5

Table 1.2 n/p-type contacts and the Schottky barrier height (Φ_B) values for multilayer MoS_2 devices with various metals whose work function (Φ_m) reported in the literature. 12

Table 3.1 MoS_2 FET design parameters. Major device dimensional parameters adapted from Ref. [66]. and multilayer MoS_2 related parameters for simulation. m_0 is the electron mass from Ref. † [21], ‡ [26], § [81]. 26

Table 4.1 MoS_2 dual-gated FETs design parameters. All the data are taken from Ref. [66], † [21], ‡ [26], § [81]. 41

Chapter 1

Introduction

1.1 History of 2D Materials

Since its proposal by Gordon Moore in April 1965, Moore's Law has described the trend that the number of transistors on integrated circuits (ICs) doubles approximately every two years. Although it is not a physical law or a law of nature in the traditional sense, Moore's Law has been true for decades. Moore's predictions were accurate and valuable, driving technological innovations and economic growth in the second half of the twentieth century. However, in recent years, the rate of doubling has slowed down due to various technological and physical limitations.

In the traditional silicon-based semiconductor industry, the line width on silicon wafers has reached the nanometer scale (10^{-9}m), equivalent to the size of only a few molecules. In this case, the physical and chemical properties of the material will undergo significant qualitative changes. As the channel length continues to scale down, new challenges emerge, including diminished low carrier mobility, heightened heat generation, and short channel effect [1]. Scientists and engineers have thought of many ways to continue Moore's Law. Despite concerted efforts by scientists and engineers to continue Moore's Law, focusing on technological advancements such as enhanced integration architectures and optimized processes, as well as novel device architectures like fin field-effect transistors (FinFETs) and complementary field-effect transistors (CFETs) [2], it has become evident that these approaches cannot fully resolve the issue. The next generation of electronic devices requires the next generation of advanced materials.

Researchers turned their attention to 2D materials, a class of atomically thin substances with distinct electrical, mechanical, and optical properties. Graphene, transition metal

dichalcogenides (TMDCs), and black phosphorus are the most prominent examples of the 2D materials family, making them highly promising for a wide range of applications, including nanoelectronics, photonics, and beyond. Among the numerous combinations of materials within the realm of TMDC semiconductors, molybdenum disulfide (MoS_2) stands out as a typical material, naturally forming a layered crystal[3, 4]. There are reviews simmarizing and commenting on its transistor functionality [5, 6, 7] and the observation of enhanced photoluminescence properties [8, 9, 10].

The origin of Molybdenum disulfide (MoS_2) can be traced back to the late 18th century when Peter Jacob Hjelm [11], a Swedish chemist, first isolated molybdenum metal. In the early stage, MoS_2 was utilized in bulk form for various industrial applications. It was not until 1923 when researchers began to understand the layered structure of Transition metal dichalcogenides (TMDCs) [12], that MoS_2's unique properties were rediscovered as a crucial member of the TMDCs family, Robert Frindt first report on the success synthesis and characterization of ultrathin MoS_2 (less than 100A) using adhesive tape in 1963 [13]. Then the monolayer MoS_2 suspensions were first fabricated by intercalation with lithium by Per Joensen in 1986 [14]. Interest in two-dimensional (2D) materials, including MoS_2, Surged again in the early 2000s following the emergence of graphene until nowadays.

1.2 Structure and Properties of MoS_2

TMDCs including MoS_2, are prominent quantum materials composed of stacked two-dimensional (2D) atomic layers, bound together through van der Waals interaction [15, 4]. These materials encompass diverse material types, including metals, semimetals, superconductors, semiconductors, and oxides. They are typically represented as MX_2, where M and X represent a transition metal atom (Ti, Zr, Hf, V, Nb, Ta, Mo, W, Tc, Re, Co, Rh, Ir, Ni, Pd, Pt)and a chalcogen atom (S, Se, Te), respectively. Researchers have extensively investigated layered TMDCs heterostructures for applications in both fundamental material science and practical engineering. Recent reviews have highlighted the attractive advantages of TMDCs, underscoring their thickness-dependent properties [16, 4]. The process of exfoliating bulk TMDCs into ultrathin 2D monolayer triggers substantial changes across its intrinsic bandstructure, charge mobility, near-infrared absorption, magnetism, mechanical strength, thermal conductivity, electrical properties, and numerous other properties [17].

Among TMDC semiconductors, molybdenum disulfide (MoS_2) is particularly notable for its natural layered crystal structure and distinct semiconductor properties [3, 4]. Each layer consists of a plane of Mo (+4) atoms sandwiched between S (-2) ions bonded together by covalent bonds (Fig. 1.1 (a)), with layers held together by relatively weak van der Waals

forces [18]. Monolayer MoS_2 exhibits two phrases: a metallic octahedral crystal symmetry configuration (1T) and semiconducting trigonal prismatic polytype (2H) [19] as shown in Fig. 1.1 (b). This semiconductor nature enables the application of MoS_2 in next-generation optoelectronic devices.

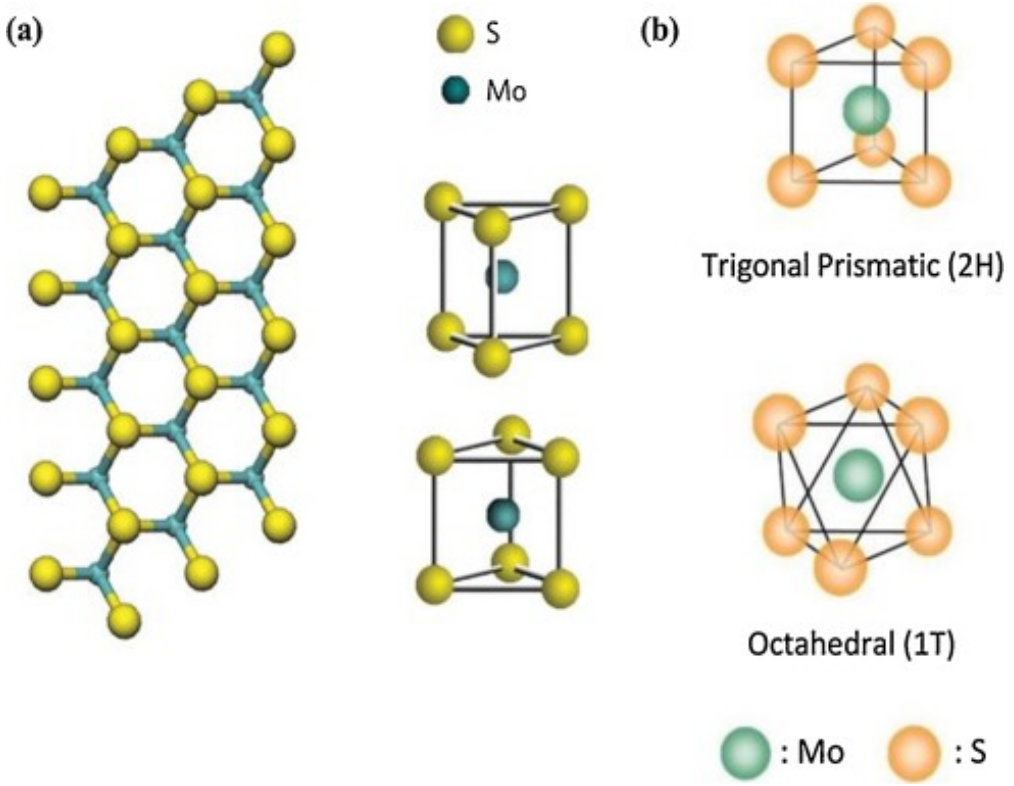

Figure 1.1: Crystal structures of MoS_2: (a) Top view of MoS_2 monolayer hexagonal crystal structure. (b) Trigonal prismatic (2H) and octahedral (1T) unit cell structures [19].

Fig.1.2 shows the band structures of the band structure of 2H-MoS_2 plotted by density function theory (DFT) [20]. Remarkably, the number of layers can dramatically impact electronic and optical properties. It can be found that upon varying thickness from bulk to monolayer, the position and value of the lowest edge of the conduction band and the highest edge of the valence band both change with decreased thickness. The electrical properties of Bulk MoS_2 are determined by an indirect transition with a relatively small band gap of 1.3 eV, while monolayer MoS_2's band structure shifts towards a direct electronic transition from the K and K' points of the Brillouin zone, resulting in an energy band gap of 1.8

eV [21, 22, 23]. This phenomenon can be attributed to an increase in the indirect band gap due to a significant quantum confinement effect in the out-of-plane direction, while its direct band gap is minimally affected as the material's dimensions are reduced to a few layers [10]. It is reported that the direct K $\rightarrow$ K' gap is 1.79 eV and the indirect $\Gamma \rightarrow$ Q gap is 2.03 eV [24], thus making the direct band gap becomes more pronounced.

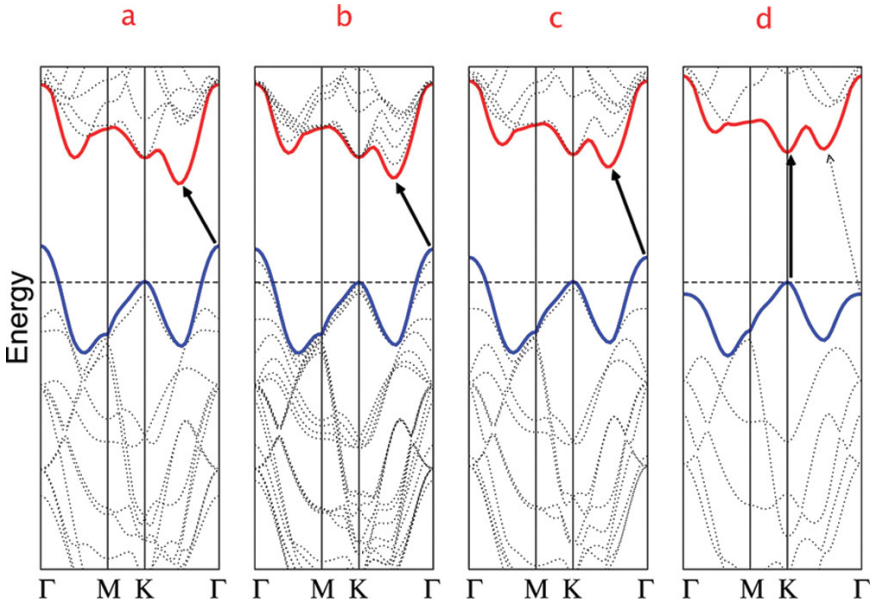

Figure 1.2: Calculated band structures of (a) bulk MoS_2, (b) quadrilayer MoS_2, (c) bilayer MoS_2, and (d) monolayer MoS_2. The solid arrows indicate the lowest energy transitions. Bulk MoS_2 is characterized by an indirect bandgap. The direct excitonic transitions occur at high energies at K point. With reduced layer thickness, the indirect bandgap becomes larger, while the direct excitonic transition barely changes. For monolayer MoS_2 in d, it becomes a direct bandgap semiconductor. This dramatic change of electronic structure in monolayer MoS_2 can explain the observed jump in monolayer photoluminescence efficiency.[20]

The direct band gap in monolayer MoS_2 is favored for optical device applications as the direct band gap allows for minimum energy required for electron transitions to occur at the same momentum, making it highly efficient for optical processes [25]. Multilayer MoS_2 remains prominent in the application of electronic devices. First, monolayer MoS_2 obtained through either mechanical exfoliation or chemical vapor deposition (CVD), tends to have low yield, more cost, and inferior quality. In contrast, multilayer MoS_2 offers superior

Table 1.1: Comparison of semiconductor properties between monolayer MoS_2 and multilayer MoS_2. [21, 26, 27]

Properties	**Monolayer**	**Multilayer (bulk)**
Bandgap (E_g)	1.8 eV	1.3 eV
Electron affinity (χ)	4.7 eV	4.0 eV
Dopant concentration (N_D)	4×10^{16} to $1.4 \times 10^{19} cm^{-3}$	
Permittivity (ε)	4.2 ε_0	11 ε_0
Electron effective mass (m_e)	0.5 m_0	0.56 m_0
Hole effective mass (m_h)	0.5 m_0	0.52 m_0
Mobility (μ)	1 to 10 $cm^2V^{-1}s^{-1}$	8 to 30 $cm^2V^{-1}s^{-1}$
SRH lifetimes (τ)	1 ns	0.1 ns

current-carrying capacity due to four times the carrier mobility [26]. More details of the comparison between multilayer MoS_2 and monolayer MoS_2 can be found in Table 1.1.

1.3 MoS_2 Field-Effect Transistors

Field-effect transistors are fundamental components in advanced electronic devices, enabling the control of two distinct on/off states. They are essential and basic building blocks for electronic devices application of tactile sensors [28], neuromorphic computing [29] and quantum computing [30]. MoS_2 exhibits exceptional electrostatic response to gate control due to its atomic thickness [31, 32, 6], and it also demonstrates excellent immunity to short channel effects (SCE). Therefore, MoS_2 has been widely investigated as a channel material for FETs including tunnel FET (TFET) [33], Schottky barrier FET (SBFET) [34] and junction FET (JFET) [35].

A significant milestone was achieved by B. Radisavljevic et al.[36] in 2011 with the fabrication of the first MoS_2 FET, with monolayer MoS_2 as channel material demonstrates a high room temperature current on/off ratio (I_{ON}/I_{OFF}) of 10^8, a small subthreshold swing (SS) of 74 mV/decade and a high mobility of $cm^2V^{-1}s^{-1}$. After that, various MoS_2 FET designs emerged. The structures of MoS_2 FET can be mainly categorized into three configurations based on the position of the gate electrode: namely back-gated MoS_2 FET, top-gated MoS_2 FET, and double-gated MoS_2 FET. The illustration of these three configurations is shown in Fig.1.3[6].

In the context of conventional back-gated devices, silicon has been the primary back-gate material, often paired with SiO_2 as the gate dielectric due to its ease of fabrication.

However, the use of SiO_2 as a gate dielectric material leads to poor mobility and large hysteresis[6]. According to Lee et al [37], their flexible and transparent MoS_2 FET addressed these issues by employing hBN as a dielectric material, exhibiting mobility up to 45 $cm^2V^{-1}s^{-1}$ and reduced hysteresis. Similarly, Cho et al. [38] also achieved minimizing hysteresis by employing atomic layer deposition (ALD) of Al_2O_3 as bottom gate dielectric, showing a hysteresis of only 0.86 V, compared to the large hysteresis of 45.0 V observed in MoS_2 FET with SiO_2.

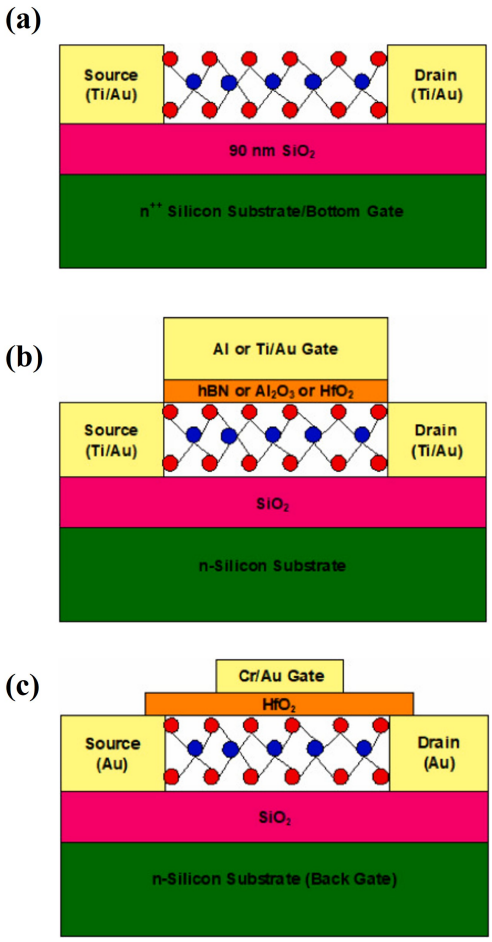

Figure 1.3: Device structure of a (a) back-gated MoS_2 FET, (b) top-gated MoS_2 FET, (c) double-gated MoS_2 FET [6].

Top-gated MoS_2 FET offers advantages over back-gated MoS_2 FET as they can regulate

individual MoS_2 FET operations[6]. Moreover, when incorporating high-k dielectrics, top-gated MoS_2 FET exhibits improved electrical performance, including lower subthreshold swing benefiting from effective screening effects. In a comparative study conducted by Chen et al [39]. P(VDF-TrFE-CFE) top Top-gated MoS_2 FET demonstrated superior electrical performance compared to SiO_2 back-gated MoS_2 FET, with a high/off ratio reaching up to 10^6 and a mobility to be 51.94 $cm^2V^{-1}s^{-1}$. So far, experimental results have confirmed that the integration of high-k dielectric materials such as Al_2O_3 or HfO_2 [40] as top-gate dielectrics enhances mobility and improves subthreshold swing. However, it is important to note that top-gated MoS_2 FET suffers from the complexity in interface engineering, the presence of dangling bonds on the MoS_2 film surface limits the uniform deposition of thin-film high-k dielectric material [41], which may require more engineering efforts.

Dual-gated MoS_2 FET denotes a structure featuring both a top gate and a bottom gate simultaneously. In the device designed by B. Radisavljevic et al., a 30 nm layer of HfO_2 was deposited on top of MoS_2 to serve as the top-gate dielectric material [36], while SiO_2 was used as the back gate dielectric material. This configuration allows each gate to independently modulate the conductivity of the channel, enabling more precise manipulation of the transistor's behavior.

While experimental studies have extensively examined MoS_2 FET. In parallel, there is a lot of literature worked on modeling the electrical performance of MoS_2 FET [42, 43, 44, 45, 46, 47, 48]. several studies emphasized on the analysis of how devices perform when channel length scales to the nanoscale(10nm) [45, 46, 47, 48], namely the ability of MoS_2 FET against short channel effect. As highlighted by Zhang et al. [46], their simulation using Synopsys Sentaurus found that MoS_2 FETs exhibit better suppression of the short channel effect when compared to silicon-based FinFET, demonstrating its advantages over conventional FETs. Others investigated the impact of various device configurations, including dielectric material, and doping concentration, on key device performance such as on/off ratio, threshold voltage, subthreshold swing [42, 43, 44]. Furthermore, an analog circuit simulation conducted by Wei et al. [49] aimed to evaluate the performance difference between MoS_2 FET and silicon FinFET when operating as common-source amplifiers in circuit, their findings show significant advantages in employing MoS_2 over silicon transistors in analog circuits, as evidenced by quantitative measures of voltage gain, power consumption, chip area, and resilience to process variations.

1.4 MoS_2 Photodetectors

Photodetectors are optoelectronic devices that are sensitive to light. Photons with energy larger than the material bandgap excite electron-hole pairs. [10] With appropriate mechanisms to separate these generated carriers, they can be collected by terminals, thereby converting optical signals into electrical signals. Monolayer MoS_2 is considered a promising candidate for next-generation flexible and transparent photodetectors. Notably, it exhibits a strong light absorption capability, absorbing up to 5-10% of incident light [50]. This is approximately one order of magnitude higher than that of GaAs and Si. This outstanding absorption is attributed to its direct bandgap nature and the strong excitonic effect arising from low dimensional structure.

Shen et al. [51] compared the photoresponsivity of nanoflake MoS_2 (t = 45 nm) with bulk MoS_2 (t = 53 μm), a responsivity of 20-30 A/W is reported for nanoflake MoS_2, which is higher than those of that of bulk MoS_2 (0.001-0.009 A/W) for over three orders of magnitude. They utilized a simple photodetector structure, a photoconductor, which consists of two terminals with MoS_2 as the channel in the middle as shown in Fig.1.4(a), external bias is applied to separate photo-generated carriers. Based on the photoconductor, to surpass dark current, as shown in Fig.1.4(b), an additional gate terminal is introduced to enable the device to deplete the channel of carriers when light is off, thus transforming it into a transistor. One of the initial high-performance monolayer MoS_2 phototransistors was reported by Lopez-Sanchez et al. [52] in 2013, monolayer MoS_2 was mechanically exfoliated and transferred to SiO_2/Si substrate, the device demonstrates a high photoresponisvity of up to 880 A/W, which can be attributed to improved mobility and contact quality. While using a single MoS_2 in photoconductor and phototransistor devices as the channel material is simple to manufacture, the carrier separation in these structures is considered low in efficiency. Moreover, a relatively large bias is required to sustain electric potential between the anode and cathode or to deplete the channel. For instance, V_{DS} and V_{GS} need to be 8 V and -70 V to achieve high responsivity [52], respectively. A more efficient photo-generated carriers separation mechanism relies on the built-in voltage instead of external voltage, the formation of built-in voltage is achieved by p-n junctions between MoS_2 and other 2D material, or Schottky junctions between MoS_2 and metal, such devices are known as photodiode as shown in Fig.1.4(c). Cheng combined p-type monolayer tungsten diselenide (WSe_2) and n-type multilayer MoS_2 to create a vertical heterostructure [53], which exhibits fast photoresponse and external quantum efficiency of up to 12%. Other 2D materials investigated for forming high-quality heterojunction with MoS_2 in photodetector applications include other TMDCs like $MoTe_2$ [54], WS_2 [55], and gapless graphene [56].

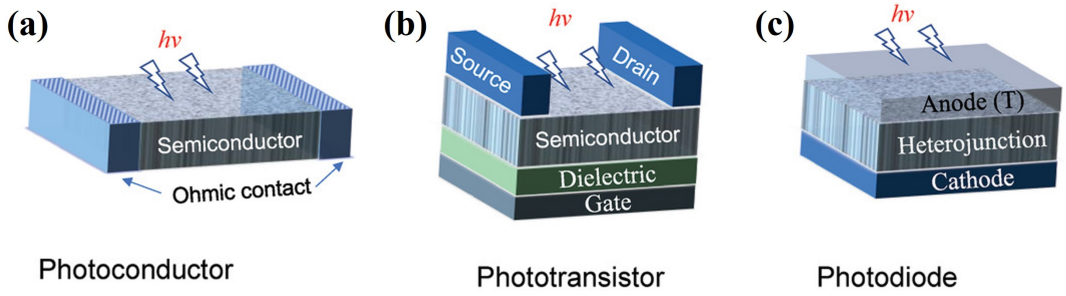

Figure 1.4: The device structure of a (a) Photoconductor, (b) Phototransistor, (c) Photodiode [57].

1.5 Fermi-Pinning Effect

Though huge achievements have been achieved in the field of MoS_2-based devices, a major challenge still lies in the strong Fermi-level pinning effect (FLP) at the metal-MoS_2 interface [58, 59], which leads to untunable Schottky barrier height(Φ_B) thus introducing unexpected contact resistance(R_c) to circuits and the reduced mobility compared to ohmic contact.

In the normal case, the Φ_B for electron $\Phi_{B,n}$ is defined as the difference between metal work function Φ_m and electron affinity χ of the semiconductor according to the Schottky-Mott rule.

$$\Phi_{B,n} = \Phi_m - \chi \tag{1.1}$$

In equilibrium, $\Phi_{\mathrm{B,n}}$, and Φ_B for holes, $\Phi_{\mathrm{B,p}}$, sum to the band gap energy.

$$E_g = \Phi_{\mathrm{B,n}} + \Phi_{\mathrm{B,p}} \tag{1.2}$$

An Ohmic contact occurs when either the $\Phi_{\mathrm{B,p}} = 0$ eV (Fig.1.4(a)) or $\Phi_{\mathrm{B,n}} = 0$ eV (Fig.1.4(b)) since either holes or electrons face no barrier, the I-V curve of an Ohmic contact is non-rectifying and appears as a straight line as shown in Fig.1.4(c). In contrast, a Schottky contact is characterized by non-zero barrier heights for both holes and electrons

(Fig.1.4(d)), resulting in a rectifying I-V curve that allows one-way conduction, as shown in Fig.1.4(e). Fig.1.4(f) depicts the I-V curve of a double Schottky barrier device [60], where both electrodes form Schottky contact, a configuration commonly found in practical two-terminal or three-terminal devices.

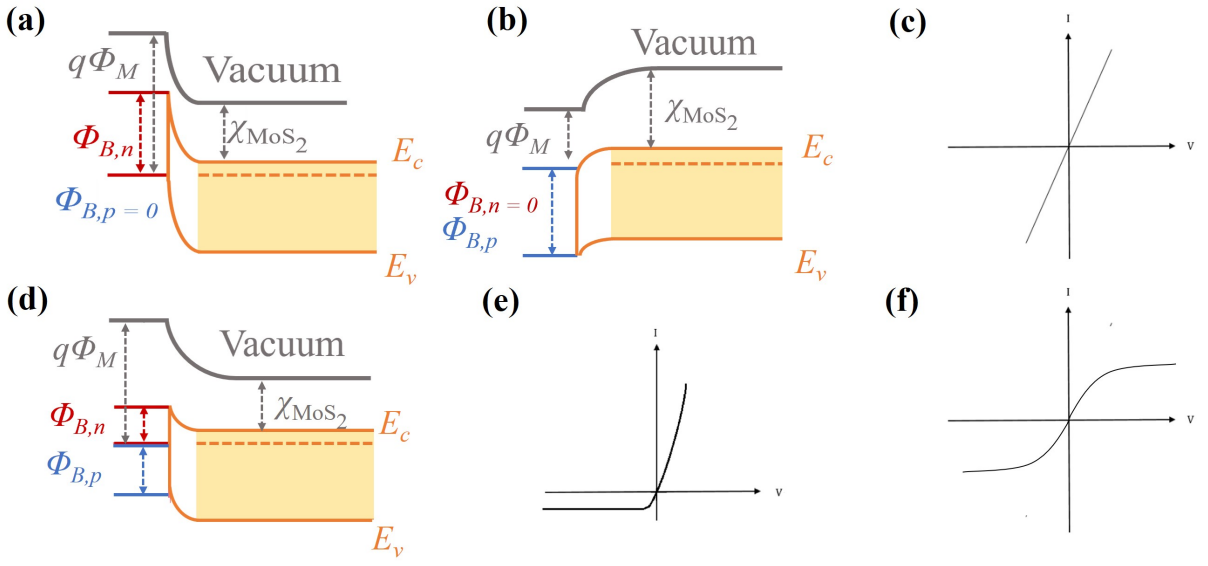

Figure 1.5: Energy diagrams of a p-type Ohmic contact (a), n-type Ohmic contact (b). (c) Schematic I-V characteristics of Ohmic contact. (d) Energy diagrams of a Schottky contact, for Schottky contact, it's n-type if $\Phi_{B,n} < \Phi_{B,p}$, it's p-type if $\Phi_{B,p} < \Phi_{B,n}$. Schematic I-V characteristics of single Schottky contact (e) and double Schottky contacts (f).

Theoretically, the type of contact - whether Ohmic or Schottky, whether p-type or n-type depends on the choice of metals for a given channel material. However, 2D materials are an exception. MoS_2, in equilibrium, has the intrinsic Fermi-energy ($E_{F,i}$) that sits in the middle of the bandgap energy shown in Fig.1.6(a). According to the bandgap energy of 1.3 eV for multilayer or bulk MoS_2 and $E_{F,i}$, metals with a low Φ_m (e.g. Sc, Ti) are expected to form n-type contacts, while those with a high Φ_m (e.g. Au, Pd, Pt) may yield p-type contacts as shown in Fig.1.6(b).

However, due to the nature of stacked atomic layers of 2D material, there are plenty of dangling bonds distributed at the MoS_2-metal interface, so MoS_2 easily suffers from these defects state than bulk materials, which results in FLP that deviates SBH from the prediction of Schottky-Mott rule. In the term of MoS_2, the existence of FLP positions the

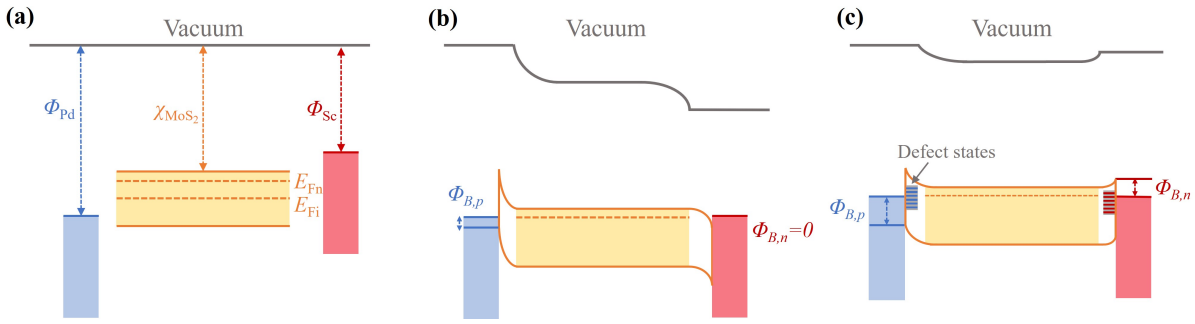

Figure 1.6: (a) Energy diagrams of Sc (Φ_{Sc} = 3.5 eV) and Pd (Φ_{Pd} = 5.1 eV) and a multilayer MoS_2 with electron affinity χ_{MoS_2} = 4.0 eV and a bandgap energy of $E_g = E_c – E_v$ = 1.3 eV, where E_c and E_v are conduction band energy and valence band energy before contact. Diagrams of band alignment when Pd (blue) and Sc (red) metal contacts to multilayer MoS_2 without (b) and with (c) Fermi level pinning effect after contact.

Fermi level of the metal line up close to the conduction band while Φ_m of metal contacts can only play a small role in the determination of Φ_B, the energy band alignment considering FLP is shown in Fig.1.6(c). As a result, the Schottky barrier inevitably forms at the metal-semiconductor interface, and FLP leads to a relatively low $\Phi_{B,n}$ [61]. In addition, under ambient conditions, the natural MoS_2 empirically is always found to be n-doped. The exact cause of this unintended n-doping in MoS_2 has not been determined. However, it is likely due to surface defects, additional carbon doping during the growth [61], or oxygen doping from a SiO_2 substrate [62]. Its typical doping concentrations range from 4×10^{16} to $1\times10^{19}/cm^3$ [26]. As a result, an electron accumulation channel can be easily formed with low resistance even when employing high work function Φ_m metals [63]. On the other hand, the associated $\Phi_{B,p}$ is consistently large from the valence band, coupled with its relatively large bandgap energy of 1.3 eV (monolayer) or 1.9 eV (bulk), these factors hinder the formation of the inversion channel (p-type) for hole injection. It greatly suppresses the pathway to build p-type FETs or ambipolar FETs using MoS_2.

However, despite the mechanism of FLP has been revealed, the precise determination of the Φ_B always depends on the quality of interfaces between MoS_2 and contact metals [64]. Some empirically determined Φ_B are listed in Table 1.2, showing significant discrepancies across various experimental observations even for the same metals. These discrepancies can be attributed to the actual processing conditions during metal deposition, the common metal deposition technique includes evaporation and sputtering. Noteworthy is the work of Wang et al. [65], who developed a strategy aimed at achieving pure p-type and ambipolar

Table 1.2: n/p-type contacts and the Schottky barrier height (Φ_B) values for multilayer MoS_2 devices with various metals whose work function (Φ_m) reported in the literature.

Metal	**Metal deposition method**	**Contact type**	Φ_m **(eV)**	$\Phi_{B,n(p)}$ **(eV)**	**References**
Sc	e-beam evaporation	n	3.5	0.03	[66]
Sc	e-beam evaporation	n	3.5	0.05	[67]
Ti	e-beam evaporation	n	4.3	0.1	[68]
Ti	e-beam evaporation	n	4.3	0.05	[66]
Ti	e-beam evaporation	n	4.3	0.13	[67]
Ni	e-beam evaporation	n	5.0	0.15	[66]
Ni	e-beam evaporation	n	5.0	-	[69]
Au	e-beam evaporation	n	5.1	0.126	[64]
Au	sputtering	n	5.1	0.45	[70]
Pd	e-beam evaporation	n	5.4	0.4	[64]
Pd	e-beam evaporation	n	5.4	0.25	[63]
Pd	sputtering	p	5.4	-	[71]
Pd	e-beam evaporation	p	5.4	0.5	[65]
Pt	e-beam evaporation	n	5.9	0.23	[66]
Pt	e-beam evaporation	p	5.9	0.75	[65]

devices on 2D MoS_2 based on industrial-compatible electron-beam evaporation. This approach mainly involved the optimization of various electron-beam evaporation parameters, including deposition rate, base vacuum pressure, and temperature control.

1.6 Outline of the Thesis

The experimental exploration of MoS_2-based Field-Effect Transistors (FETs) has provided extensive insights. However, it becomes apparent that the establishment of numerical modeling as a tool to predict the performance of devices is also important, serving as a complementary approach. In this work, we aim to present a thorough simulation study focused on evaluating the electronic and optical performance of MoS_2-based devices. A key challenge addressed is the inevitable Schottky barrier formation at the MoS_2/semiconductor interface due to the Fermi-level pinning effect. Therefore, our simulation incorporates this Schottky barrier and assesses its impact on the device's electronic and optoelectronic performance.

This Chapter provides an overview of MoS_2 as well as its state-of-the-art applications of field effect transistors and Photodetectors. In particular, the Fermi pinning effect that

induces the Schottky barrier is emphasized.

Chapter 2 begins by presenting the theoretical background of the drift-diffusion model, which includes three basic equations and is the most classical framework used to describe the behavior of carriers (electrons and holes). In particular, since our focus is Schottky barrier-based devices, the physics behind the boundary condition at metal contact is also stated. Subsequently, the theoretical background of optoelectronic modeling is introduced. In the end, a simulation scheme is presented to illustrate how simulation tools handle the mathematical partial differential equations inherent in electronic and optoelectronic modeling.

Chapter 3 focuses on the electrical performance simulation of Schottky barrier MoS_2 FETs. Initially, simulation results are compared with experimental data to validate the model. Then with varying Schottky barrier height, a transition from n-type conduction to p-type conduction is observed and analyzed in the simulated device. Based on that, an ambipolar MoS_2 FET is designed by utilizing asymmetric metals to facilitate the transport of holes and electrons. Additionally, an analysis of the tunneling effect through the Schottky junction and the variation in electrical performance depending on the contact area is also included.

Chapter 4 proposes a dual-gate MoS_2 FET with asymmetric contact. This configuration enables reconfigurability, either a $p-n$ junction or a $n-p$ junction can form by electrostatically doping when appropriate gate voltages are applied. Such versatility makes it promising for application in photodiodes. Furthermore, the optoelectronic performance simulation of the dual-gate MoS_2 FET under incident light across various power densities reveals a photoresponsivity of 24.2 mA/W. Finally, a detailed study is conducted to analyze the contribution of the $p-n$ and Schottky junction to photogenerated carrier separation as a function of gate voltage.

Chapter 5 integrates the results of the simulation studies. it draws conclusions based on these findings and states the prospects of MoS_2-based transistor design.

Chapter 2

Theoretical background

When exploring the electrical and optoelectronic performance of MoS_2-based devices, the drift-diffusion model serves as the cornerstone of the electrical simulation while Maxwell's equations are prerequisites for studying photosensitive devices. This section will introduce the three fundamental equations involved in the drift-diffusion model, and essential boundary conditions, and provide a brief overview of Maxwell's equations. Additionally, it will describe how these equations are refactored and applied in numerical methods.

2.1 Drift-Diffusion Model

The development of the Drift-Diffusion model can be traced back to the 1950s [72], where it was initially applied to simulate the electrical performance by simulating the carrier transport behavior. Even today, When dealing with large-scale devices with channel lengths in the micrometers or hundreds of nanometers range, the conventional drift-diffusion model remains effective. The Drift-Diffusion model describes two fundamental processes consisting of the total current density of electrons and holes: drift and diffusion. In detail, the equations for the current density of electrons and holes are as follows:

$$J_n = q\mu_n nE + qD_n \nabla n \tag{2.1}$$

$$J_p = q\mu_p pE + qD_p \nabla p \tag{2.2}$$

where J_n and J_p are current densities for electrons and holes, respectively. μ_n and μ_p are mobility for electrons and holes, respectively. D_n and D_p are diffusion constants for electrons and holes, respectively. The first term in Equation represents the drift process, which refers to the movement of carriers in response to an electric field, depending on the mobility and carrier concentration, while the second term represents the diffusion process, which accounts for the transport of carriers caused by non-uniform distribution of charged particles in different regions, depending on the diffusion constant. The combination of the drift and diffusion process accounts for the transport physics in semiconductors.

It can be found that the analysis of semiconductor devices is inseparable from the analysis of the electrostatic field in the device. The subsequent equation comes from the electrostatics aspect, known as the Poisson equation:

$$\nabla \cdot (-\epsilon_0 \epsilon_r \nabla V) = \rho. \tag{2.3}$$

It is derived from Maxwell's equations of electromagnetism, it describes how the electric potential V in a material with relative permittivity ϵ_r with respect to the vacuum permittivity ϵ_0 is related to the charge density ρ according to Gauss' law, once the potential distribution is determined, the band diagram can be plotted accordingly. ρ in the semiconductor satisfies

$$\rho = q(p - n + N_d^+ - N_a^-). \tag{2.4}$$

Where q is the elementary charge, p and n are the hole and electron concentrations, respectively. N_d^+ and N_a^- are the ionized concentration for the donor and acceptor, respectively. It is worth noting since our all simulations are conducted under normal room temperature conditions, Complete ionization in a doped semiconductor is assumed, meaning that the concentration of ionized donors and acceptors is equal to the concentration of donor doping, N_D and acceptors doping, N_A, respectively.

The third set of equations is continuity equations, which deliver a simple interpretation: The reason for the change in particle number within a certain volume must be attributed to the net inflow and outflow of carriers. In the context of the drift-diffusion model, a particle refers to an electron or hole, the inflow of carriers is represented by the term "generation rate(G)" while the outflow of carriers is represented by the term "recombination rate(R)". Taking the relationship between current density and the carrier numbers into consideration, current density can be related to the generation and recombination of carriers. These

equations can be expressed as:

$$\frac{dn}{dt} = \frac{1}{q}(\nabla J_n) - (R - G) \tag{2.5}$$

$$\frac{dp}{dt} = -\frac{1}{q}(\nabla J_p) - (R - G) \tag{2.6}$$

Under thermal equilibrium and steady-state conditions, the carrier concentration doesn't change with time so $\frac{dn}{dt}$ and $\frac{dp}{dt}$ both equal to 0, rearranging the equations to be

$$\frac{1}{q}\nabla J_n = R - G \tag{2.7}$$

$$\frac{1}{q}\nabla J_p = G - R \tag{2.8}$$

The three constitutive equations described above form the basis of the drift-diffusion model, which is fundamental for numerical approaches in solving various classical semiconductor problems, including those encountered in our simulation.

2.2 Metal Contacts

Metal contacts act as a boundary condition for applying external voltage. Physically, the metal-semiconductor interface can form two types of contacts: ohmic and Schottky. The former ohmic contact does not add any resistance to the overall device resistance, leading to linear $I - V$ characteristics. In contrast, Schottky contact results in additional contact resistance and causes rectifying current-voltage behavior. This thesis employs the ideal Schottky contact boundary condition in numerical simulation to model the metal-to-MoS_2 interface.

Currents in a Schottky barrier junction have two components: (1) thermal currents from thermionic carrier injection over the Schottky barrier and (2) thermally assisted tunneling currents of carriers through the Schottky barrier [73]. According to the nature of the contributing currents, current transport mechanisms can be divided into three various regimes as shown in Fig.2.1: thermionic emission (TE), thermionic field emission (TFE), and field emission (FE). TE is primarily dominated by thermal currents and FE is governed

by tunneling currents, while TFE involves a combination of both thermal and tunneling currents.

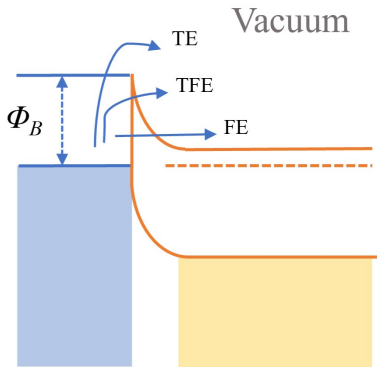

Figure 2.1: The schematic of an ideal Schottky barrier and three conduction mechanisms (TE: thermionic emission, TFE: thermionic-field emission, FE: field emission) by which an electron can pass across the barrier.

2.2.1 Thermionic Emission Model

In terms of effective recombination velocities v_n and v_p for electrons and holes, thermionic currents can be expressed as:

$$J_n = -qv_n(n - n_0), \tag{2.9}$$

$$J_p = -qv_p(p - p_0). \tag{2.10}$$

if the current flows under a bias in a non-equilibrium case. The quasi-equilibrium carrier densities of n_0 and p_0 are determined when the semiconductor Fermi energy coincides with that of metal E_{Fm} at a fixed temperature T,

$$n_0 = N_c \exp(-\frac{E_c - E_{\mathrm{Fm}}}{k_B T}) = N_c \exp(-\frac{\Phi_{\mathrm{B}}}{k_B T}), \tag{2.11}$$

$$p_0 = N_v \exp(-\frac{E_{\mathrm{Fm}} - E_v}{k_B T}) = N_v \exp(-\frac{E_g - \Phi_{\mathrm{B}}}{k_B T}), \tag{2.12}$$

in terms of the Schottky barrier height Φ_{B}, which is defined as the difference between metal work function Φ_{m} and electron affinity χ of the semiconductor and a Boltzmann constant k_B. N_c and N_v are the effective densities of states in the conduction band and valence band, respectively. The electron and hole recombination velocities v_n and v_p are calculated with effective Richardson's constants, A_n^* for electrons and A_p^* for holes in a simple relation:

$$v_{n(p)} = \frac{A^*_{n(p)} T^2}{q N_{c(v)}}. \tag{2.13}$$

2.2.2 Wentzel-Kramers-Brillouin Tunneling Model

The impact of tunneling current can't be ignored when the thickness of the Schottky barrier is comparable to or thinner than the characteristics length scale λ. The λ represents the distance required for the electric potential to diminish from metal contacts toward the semiconductor channel. This is particularly relevant in our case, as 2D materials feature a smaller λ compared to conventional bulk materials. [74, 75, 76]. For instance, for identical parameters, the typical λ is around 20 nm for silicon, but for a single layer MoS_2 it is only 3 nm. Hence, it is vital to incorporate the tunneling current effect into the simulation.

To evaluate the tunneling contribution, we employ the standard Wentzel-Kramers-Brillouin (WKB) tunneling model. with several user-defined parameters, including the effective mass of electrons (m_e^*) and holes (m_h^*), field line coordinate, boundary coordinate (spanning the tunneling boundary) and specified tunneling barrier region in geometry. The computed tunneling current adds a fractional increase, δ, to the original thermionic current:

$$\delta = \frac{q}{k_B T} e^{qV_{\max}/k_B T} \int_{V_{\min}}^{V_{\max}} e^{qV_x/k_B T} e^{-4\pi/h \int_1^2 \sqrt{2m(E_b - qV_x)} dl} dx \tag{2.14}$$

where m is the input effective mass, E_b is the conduction band edge (E_c) for electrons. The integral ($\int_1^2$) in the exponent is performed along the electric field within the tunneling barrier region, spanning from one boundary of the depletion region to the opposite boundary, while the outer integral ($\int_{V_{\min}}^{V_{\max}}$) is carried out along the electric potential axis for energy integral.

2.3 Maxwell's Equations and Light Absorption

Maxwell's equations are a set of four coupled equations. In partial differential equations form, Maxwell's equations are expressed as:

$$\nabla \cdot \mathbf{E} = \frac{\rho}{\epsilon_0} \tag{2.15}$$

$$\nabla \cdot \mathbf{B} = 0 \tag{2.16}$$

$$\nabla \times \mathbf{E} = -\frac{\partial \mathbf{B}}{\partial t} \tag{2.17}$$

$$\nabla \times \mathbf{H} = \mathbf{J} + \frac{\partial \mathbf{D}}{\partial t} \tag{2.18}$$

where E and B are the electric and magnetic fields, D and H are the electric displacement field and magnetic field intensity, respectively. Maxwell's equations form the cornerstone of classical electromagnetism. These equations describe the origin and behavior of electric and magnetic fields (equation 2.15 and 2.16), illustrating a fundamental principle: a changing electric field generates a magnetic field (equation 2.17), and a changing magnetic field generates an electric field (equation 2.18). These dynamic fields oscillate, transform into one another, and propagate through space as electromagnetic waves. The solutions to Maxwell's equations determine the spatial distribution of the electric field within complex three-dimensional structures, which is essential for computing the optical properties of materials, including absorption, reflection, and transmission.

The crucial aspect of optoelectronic devices is light absorption, described by the formula:

$$P_{\text{abs}}(r, \omega) = -\frac{1}{2}\omega |\mathbf{E}(r, \omega)|^2 \epsilon''(r, \omega) \tag{2.19}$$

where ω is the angular frequency of the electromagnetic wave, ϵ'' is the imaginary part of the dielectric function ϵ, describing the material absorption of electromagnetic energy. The real part of the ϵ, ϵ', describes the material's response to the electric field in terms of polarization and displacement of charges within the materials. The formula indicates that light absorption is determined by the interaction of the electric and magnetic fields with the material's intrinsic properties.

2.4 Simulation Scheme

2.4.1 Electrical Simulation

The electrical simulation of MoS_2 thin-film transistor is conducted using COMSOL Multiphysics, the three fundamental physical laws introduced above, forming the basis of the drift-diffusion model, are integral to the COMSOL simulation. The three equations are all partial differential equations (PDE) that are related to the space variable. However, obtaining analytical solutions to these PDEs may not always be feasible due to the complexity of the actual model. Instead, numerical methods are employed to find approximate solutions to the equations. To perform numerical methods, the overall simulation process consists of the following steps:

1. Building the physical models and geometric models of the devices to be simulated, the choice of the drift-diffusion model implements the corresponding PDE while the geometric structure defines the domain for the PDE. Initial conditions and boundary conditions are added as constraints that specify the solution behavior at certain points. The physical model and geometric model collectively form a numerical model for simulation.

2. The finite element method (FEM) discretizes (meshing) the complex overall structure into a finite number of local units of various sizes and shapes connected. An important meshing rule is that the physical field within a single unit shouldn't change dramatically or simple functions can't describe it. Therefore, mesh refinement is particularly important around special boundary conditions such as the boundary of the drain, source, and gate. Specifically, meshing should be smaller than Debye length for accurate results. Debye length is given by:

$$L_d = \sqrt{\frac{k_B T \epsilon_0 \epsilon_r}{q^2 N_{ion}}} \tag{2.20}$$

where k_B is Boltzmann's constant, T is the lattice temperature, N_{ion} is the concentration of ionized donors or acceptors. Debye length represents the distance of the electric field of carriers that can persist and should be longer than the mesh size.

3. After meshing, The physical variables, such as electric potential distribution, are discretized. Considering the discretization of potential in a two-dimensional model as an example. A simplified illustration of mesh point distribution is shown in Fig.2.2(a), where each point corresponds to a node where the potential is calculated. The potential at each

mesh point is denoted as $V_{i,j}$, where i and j represent the indices of the mesh points thus each $V_{i,j}$ can be viewed as an element in the matrix. The benefit of discretion is that derivative operators can be approximated by finite difference. considering a special graphical depiction of five adjacent cells with corresponding local potential as shown in Fig.2.2(b), which is commonly known as five-point star. The classical Poisson equation for one node located at (i,j) can be rewritten as:

$$V(i-1,j)+V(i+1,j)+V(i,j-1)+V(i,j+1)-4V(i,j)=-\frac{h^2}{\epsilon_0}\rho(i,j) \tag{2.21}$$

The equation illustrates that the local potential at node (i,j) is only dependent on the potential at four nearest neighboring nodes, with the change in charge density at node (i,j). It is worth noting that in the actual simulation process, the relationship between potentials at different mesh points is often more complicated than five-point stars due to nonuniform meshing. However, If all these relationships can be collected into a matrix A, then by vectorizing the potentials within the domain, denoted as x:

$$x=[V_{1,1}V_{2,1}V_{3,1}...V_{2,1}V_{2,2}V_{2,3}...]^T \tag{2.22}$$

the Poisson equation can be converted into a matrix-vector equation of the form:

$$Ax=b \tag{2.23}$$

where b contains the information about charge density and specific boundary conditions.

4. If the equations are linear, solving equations can be as straightforward as inverting the matrix:

$$x=A^{-1}b \tag{2.24}$$

However, in the context of semiconductor physics, the Poisson equation always exhibits nonlinear due to its coupling with carrier concentrations. While the Poisson equation

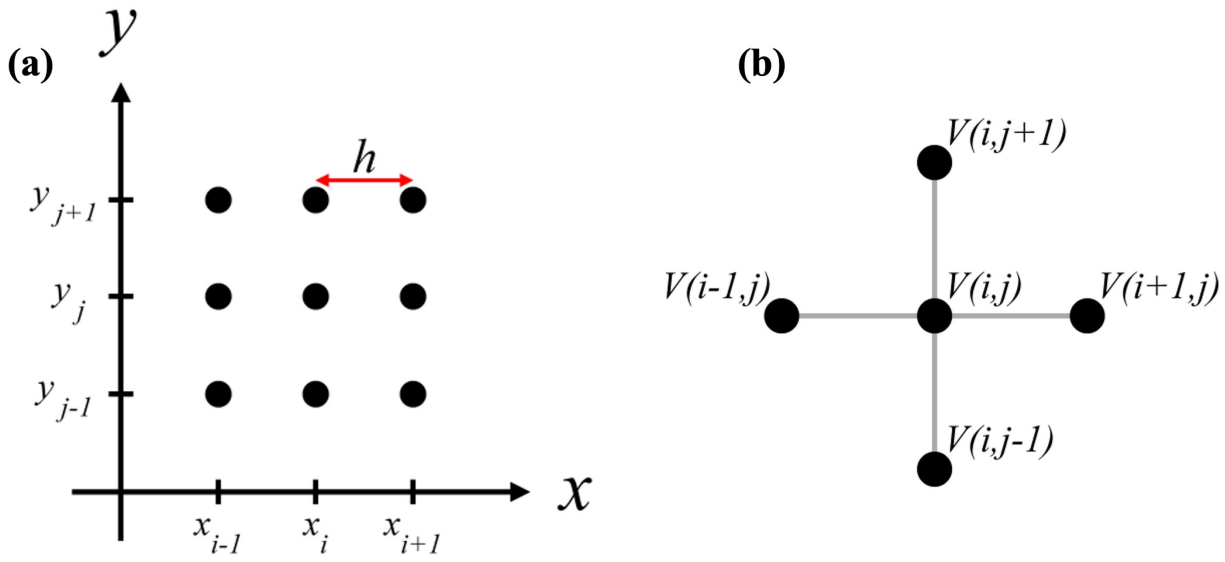

Figure 2.2: (a) Mesh points for the FDM grid (b) Computational molecule for the 5-point star [77].

relates electric potential to charge density linearly, in semiconductor devices, as carriers generate or recombine in response to the electric field created by electric potential, they affect the charge density, which in turn modifies the electric potential. This mutual dependence between the electric potential and carrier concentrations introduces nonlinearity into the Poisson equation. Mathematically, the elements in matrix A are not constant, but depend on the variable potential V. As a result, it is impossible to solve these equations analytically, The solution requires the assistance of numerical techniques like Newton's methods. To initiate the iteration loop, good initial condition values are essential, including electric potential V, electron concentration, and hole concentration.

5. During the iteration, the Poisson equation is solved in conjunction with the current continuity equation to update potential and carrier concentration. Convergence is reached once the error between the newly computed solution and the previous solution is less than a specific threshold. At convergence, the numerical solution serves as the solution to the problem.

6. With the final potential and carrier concentration solution, the electrical performance of the device can be calculated.

2.4.2 Optoelectronic simulation

Optoelectronic performance is calculated using the Lumerical method, where the simulation is also done by solving corresponding PDEs essentially. However, the choice of methods to solve PDEs may vary depending on the specific PDEs involved.

Light absorption and photocarrier generation in the simulated device are initially calculated by Lumerical FDTD. FDTD employs Finite-Difference Time-Domain (FDTD) methods, FDTD and Finite Element Method (FEM) are both numerical techniques used to solve PDEs in various fields. Unlike FEM primarily discretizes space and divides the solution domain into finite elements only, FDTD discretizes both space and time, representing fields as discrete values on a grid in both dimensions [78, 79]. when solving the problem of electromagnetic wave propagation, i.e., solving the PDEs of Maxwell's equations. The implementation of the (FDTD) method proceeds as follows.

For discretization in space dimension, similar to the FEM method, the E and H components (x,y,z in 3D space) distributed in the space are grided into one by one unit cells called Yee cell for finite difference computing as shown in the Fig 2.3 [80], where i,j,k represents the index of gird points. The E component is located at the center of the edge of the grid, while the H component is located at the center of the grid surface. this staggering of the fields in space is ideal for calculating spatial derivatives for curl terms in equations 2.17 and 2.18. This configuration ensures that each field component is centered around the locations where the curl of the other field components can be easily computed using finite difference.

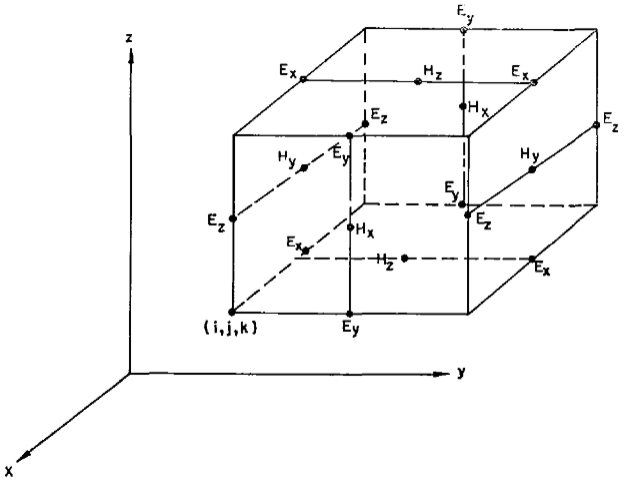

Figure 2.3: FDTD Yee Cell [80].

For discretization in time dimension, the simulation starts at time t = 0, when E and H are typically 0. Then the E and H are updated in a leapfrog way, meaning the E and H are also staggered in time. Specifically, E is updated at integer multiples of the time step (n·Δt) using the curl of H, while H is updated at half-integer multiples ((n+0.5)·Δt) using the curl of H. Magnetic and electric fields are solved alternately over time in this way.

By combing Maxwell's equations 2.17 and 2.18 finite discretion both in the time domain and space domain, the final finite-difference equations for x component of E and H for equations 2.17 and 2.18 in FDTD can be rewritten as [80]:

$$\begin{aligned}\frac{E_x^{n+1}(i,j,k) - E_x^n(i,j,k)}{\Delta t} = & -\epsilon \left(\frac{H_z^n(i,j+1/2,k) - H_z^n(i,j-1/2,k)}{\Delta y} \right. \\ & \left. - \frac{H_y^n(i,j,k+1/2) - H_y^n(i,j,k-1/2)}{\Delta z} \right)\end{aligned} \tag{2.25}$$

$$\begin{aligned}\frac{H_x^{n+1/2}(i,j,k) - H_x^{n-1/2}(i,j,k)}{\Delta t} = & -\frac{1}{\mu} \left(\frac{E_y^n(i,j,k+1) - E_y^n(i,j,k)}{\Delta z} \right. \\ & \left. - \frac{E_z^n(i,j+1,k) - E_z^n(i,j,k)}{\Delta y} \right)\end{aligned} \tag{2.26}$$

The finite difference equation corresponds to the y and z components of E and H fields can be constructed similarly. Since Maxwell's equations involve temporal derivatives, the FDTD allows for a straightforward simulation of electromagnetic wave propagation, which can be advantageous for accurately modeling the evolution of electromagnetic fields over time [79]. By comparison, FEM requires additional mathematical analysis to convert the system to another algebraic equation system. Therefore, FDTD is employed here to simulate the spatial distribution of the electric field instead of COMSOL employing FEM.

Once the absorbed optical power (P_{abs}) is determined, the photocarrier generation rate (G) is calculated by assuming each absorbed photon excites an electron-hole pair, according to the formula:

$$G = \frac{P_{abs}}{\hbar\omega} \tag{2.27}$$

Subsequently, the optical generation rate is then imported into Lumerical CHARGE to perform the electrical simulations. Similar to COMSOL, CHARGE also employs the FEM methods to solve the drift-diffusion model. The generation rates and the recombination rates serve as source and sink terms in the continuity equations (equations 2.5 and 2.6), accounting for the formation and evolution of photocurrent.

Chapter 3

Contact-Dependent Electrical Performance Simulation of Multilayer MoS_2 Transistors

Two challenges have been proposed for MoS_2 transistors: on the one hand, the device-to-device variability of Schottky barrier height, even when using the same metals, on the other hand, practical observations lack p-type or ambipolar conduction. Therefore, in this chapter, a comprehensive simulation is conducted using the simulation scheme introduced in Chapter 2 to study the contact-dependent electrical performance of Multilayer MoS_2 transistors. By sweeping the Φ_m across MoS_2 bandgap, this simulation completes the missing p-branch of MoS_2 SBFETs and establishes a reference for estimating the true Φ_B. Additionally, the ambipolar conduction behavior observed in the transistors with asymmetric metals is also investigated.

3.1 Modeling Setup and Parameters

Our simulation employs a standard transistor model with three terminals: source (S), drain (D), and backgate (G). In most scenarios. S and D electrodes are used for the injection and collection of carriers, while the gate voltage electrostatically controls the Fermi level E_{F} of the MoS_2 channel. The multilayer MoS_2 with thickness $t_{\mathrm{MoS_2}}$ channel is defined between the source and drain electrodes with length $L_{\mathrm{MoS_2}}$ and width $W_{\mathrm{MoS_2}}$. We assume that a multilayer MoS_2 region is n-type doped with a donor concentration of 4×10^{18}

cm^{-3}, reflecting its natural doping condition, which positions the Fermi level 0.1 eV below the conduction band under equilibrium at its Fermi level. The schematic illustration of the described FET is shown in Fig.3.1(a) while the corresponding meshing is presented in Fig.3.1(b). To simulate a practical MoS_2 transistor, some material values are sourced from several reports of Refs. [21, 81], and all the design parameters and material values in the simulations are listed in Table 3.1.

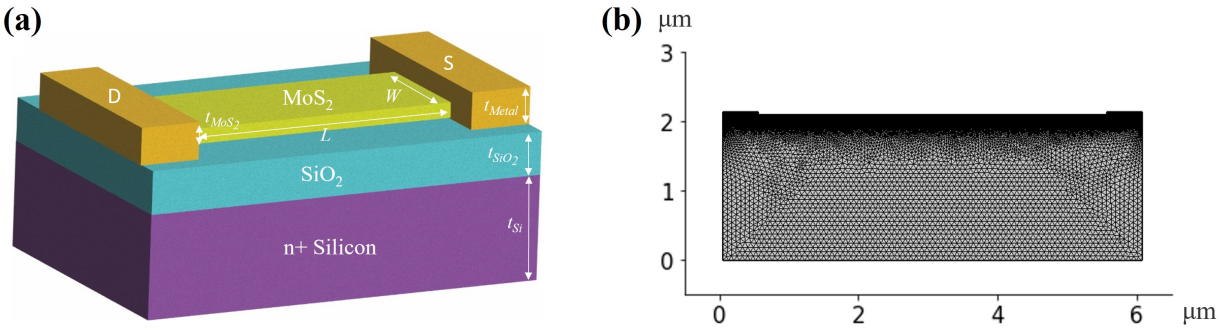

Figure 3.1: Schematic representation of the a) MoS_2-based FET device (not to scale) b) MoS_2-based FET device after meshing in COMSOL Multiphysics.

Table 3.1: MoS_2 FET design parameters. Major device dimensional parameters adapted from Ref. [66]. and multilayer MoS_2 related parameters for simulation. m_0 is the electron mass from Ref. † [21], ‡ [26], § [81].

Parameters	**Value**	**Parameters**	**Value**
t_{MoS_2} (nm)	10	m_h^*	0.5 $m_0^\dagger$
L_{MoS_2} (nm)	5000	m_e^*	0.5 $m_0^\dagger$
W_{MoS_2} (nm)	1000	N_c (m^{-3})	8.57×10^{24}
t_{metal} (nm)	50	N_v (m^{-3})	8.57×10^{24}
t_{SiO_2} (nm)	100	N_D (m^{-3})	1.4×10^{23}
t_{Si} (nm)	2000	μ ($cm^2/(V\cdot s)$)	$25^\ddagger$
T (K)	293.5	$A^*_{n(p)}(A/(K\cdot cm)^2)$	60
E_g (eV)	$1.3^\S$	$\epsilon_r(MoS_2)$	$11^\dagger$
χ_{MoS_2} (eV)	$4^\ddagger$	Contact type	Ideal Schottky

3.2 Model Verification

Our simulation aims to assess the electrical performance. To validate the accuracy of our model, we first conducted a comparative analysis with experimental data reported by Ref. [66] and our simulation results. Das et al. investigated the contact properties of scandium (Sc), titanium (Ti), nickel (Ni), and platinum (Pt) with MoS_2, whose Φ_m are reported as 3.5 eV, 4.3 eV, 5.0 eV, and 5.9 eV, respectively [66]. However, the corresponding Φ_B are found to be 0.03 eV, 0.05 eV, 0.15 eV, and 0.23 eV for these metals. This discrepancy indicates that the experimental Φ_B values do not adhere to the Schottky-Mott equation, suggesting the presence of FLP effects at these metal-MoS_2 interfaces. Therefore, to simulate the Fermi-pinning effect observed in real devices, we set the metal work function based on empirical Schottky barrier height Φ_B.

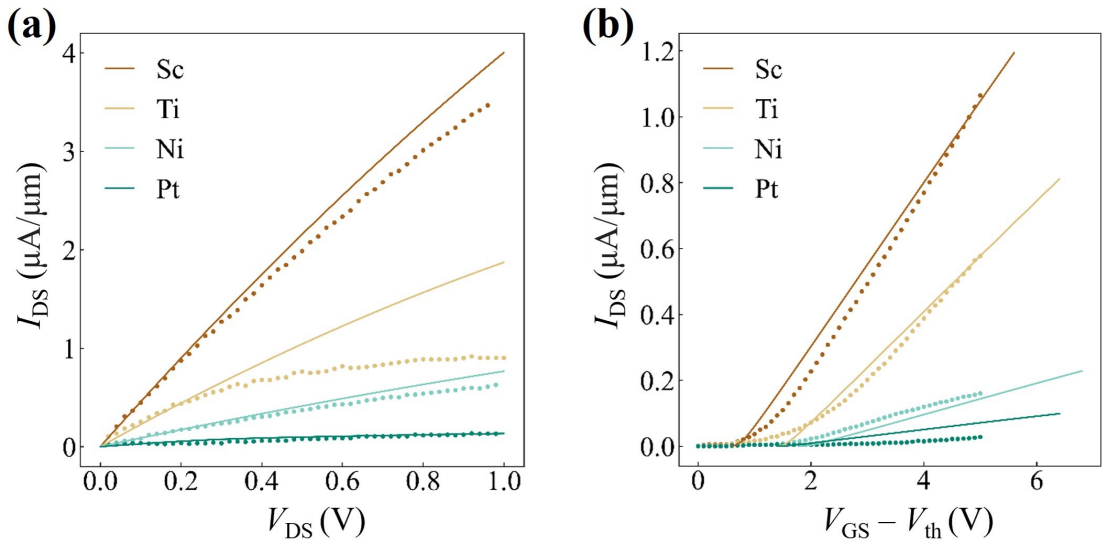

Figure 3.2: Comparison study of a multilayer MoS_2 SBFET simulation (solid lines) and experimental results (markers) with four metals (Sc, Ti, Ni, and Pt) reported from Ref. [66]. (a) Output characteristic of I_{DS} - V_{DS} for $V_{GS} = 3$ V. (b) Transconductance comparison of the I_{DS} - V_{GS} characteristic given $V_{DS} = 0.2$ V (b).

Figure 3.2 and Figure 3.3 compares experimental data (circles) reported in Ref. [66] with our simulation results (solid lines). The following transport properties are examined: I_{DS} - V_{DS} output characteristics (Fig.3.2(a)), I_{DS} - V_{GS} transfer characteristics (Fig.3.2(b)), and the Φ_B - V_{GS} of the Ni contact device (Fig.3.3). It is worth noting that the drain-

source current depicted in the figure has been length normalized along the device's width direction, given the variations in the actual widths of fabricated devices. Generally, the current is expected to exhibit proportionality with respect to the device's width.

The trend observed in Fig.3.2(a) shows that larger I_{DS} flows for smaller Φ_{B} due to metal contacts with smaller Φ_{m}. This observation aligns well with corresponding experimental plots. The simulated V_{DS} - I_{DS} for Sc, Ni, and Pt show excellent quantitative agreement with experimental data. However, the slopes of the simulated V_{DS} - I_{DS} are slightly larger than the experimental corresponding plots without exception. This discrepancy can be attributed to the presence of series resistance introduced in addition to the intrinsic material resistance and contact resistance during the fabrication process. In addition, the discrepancy between the simulation and experiment for Ti is noticeably large for high V_{DS} values, which is reflected in the smaller-than-expected saturation voltage in actual fabrication. A possible explanation for this phenomenon is the degradation of carrier mobility under high external voltage bias for this specific device, which is often related to velocity saturation where carriers cannot increase their speed further despite an increase in the electric field. Overall, the hypothesis also partially verifies that Sc, Ni, and Pt are the metals that can form the best contacts with MoS_2 with minimal unwanted resistance introduction.

MoS_2 functions as a naturally n-doped semiconductor and n-type metals with Fermi-level closer to the conduction band of MoS_2 are used as contacts. Consequently, the transfer characteristics (Fig.3.2(b)) exhibit electron dominated injection. The observed discrepancy in the transfer characteristics between experimental and simulated results manifests in the nearly identical slopes for the same metal but with a shift in gate voltage, this is due to the different threshold voltages determined in the real experiments and simulations. The threshold value V_{th} required to turn on the channel varies depending on the metal contact in the experiment, with values of -6.0, -1.0, 1.5, and 4.0 V for Sc, Ti, Ni, and Pt, respectively. However, in theory, the V_{th} remains unaffected by the actual Φ_{B} as it is typically reached in SBFET when the conduction band edge aligns with the source Fermi level [76]. This point is supported by the simulation observation, where V_{th} is consistently found to be -0.8 V regardless of Φ_{B}. In general, predicting V_{th} quantitatively for a specific device is challenging without knowing all the device details. Instead, we compare the transconductance ($g_{\mathrm{m}} = \partial I_{\mathrm{DS}}/\partial V_{\mathrm{GS}}$) of the I_{DS} - V_{GS} plots. We observe good agreement between simulation and experimental results.

In addition, we examine V_{GS}-dependent Φ_{B} values for the Ni contact device in Fig.3.3. We extract the Φ_{B} directly from the band diagrams at the metal-MoS_2 interface, then compare them with experimental data calculated using the equation $I_{\mathrm{DS}} = A^* T^2 \exp(q\Phi_{\mathrm{B}}/k_{\mathrm{B}}T)[1-\exp(qV_{\mathrm{DS}}/k_{\mathrm{B}}T)]$ in conventional thermionic emission theory, where A^* is the Richardson constant [82]. The significance of the V_{GS}-dependent Φ_{B} plot lies in its revealing informa-

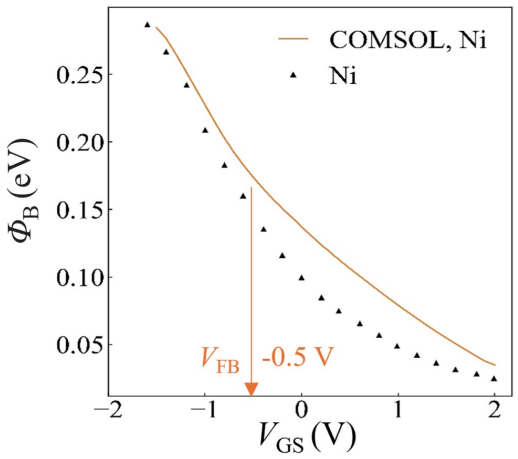

Figure 3.3: Comparison study of a multilayer MoS_2 SBFET simulation (solid lines) and experimental results (markers) with four metals (Sc, Ti, Ni, and Pt) reported from Ref. [66]. Schottky barrier height (Φ_B) as a function of applied V_{GS} for the Ni contact device, with a simulated V_{FB} of -0.5 V.

tion about the contribution of different current components. For gate voltage below flat band voltage V_{FB} (more information about V_{FB} is discussed in the next section), Φ_B exhibits a linear response to V_{GS}, indicating the presence of only thermionic emission current (TE). However, when the TFE region is reached for V_{GS} ¿ V_{FB}, the linear relationship between Φ_B and V_{GS} no longer exists[82]. The Φ_B at this V_{FB} is believed to reflect the actual Φ_B[76]. Our V_{FB} value from the simulation is -0.5 V, which is the same as the reported value of -0.5 V in Ref. [66]. These results validate the accuracy of our model in simulating the electrical performance of FETs.

3.3 Tunneling Currents in MoS_2 SBFETs

Electrons or holes can tunnel through a barrier instead of climbing over it, leading to tunneling effects. The key parameter that determines the tunneling possibility is the shape of the barrier region, including barrier height and barrier region. V_{GS} can adjust the barrier region, thereby influencing the contribution of tunneling current to the total current. The dependence of tunneling current on V_{GS} is examined here. To better visualize the roles of hole tunneling and electron tunneling, a $\Phi_{B,n} = \Phi_{B,p} = 0.65$ eV is chosen as it sits in the middle of the band gap of MoS_2, generating comparable electron and hole branches.

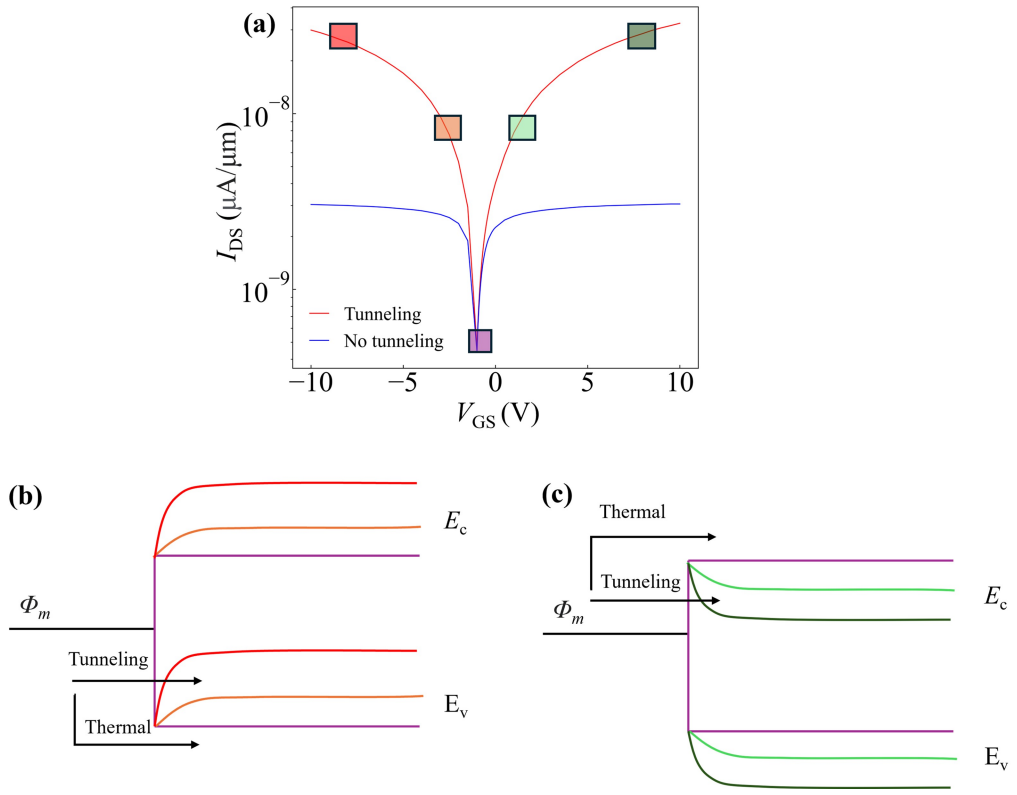

Figure 3.4: (a) Comparison between the simulation results with and without tunneling current contribution as a function of V_{GS}, V_{DS} = 0.2 V. The corresponding band diagram at different V_{GS} from (a). (b) V_{GS}: -10 V to -1.1 V. (c) V_{GS}: -1.1 V to 10 V.

Fig.3.4 (a) presents a comparison between the I_{DS} - V_{GS} with tunneling effect and without tunneling effect. The overall performance of tunneling current can be explained from the perspective of the band diagram. At the contact, the band diagram transitions from upward bending to downward bending as V_{GS} changes from -10 V to 10 V (Fig.3.4 (b) and (c), respectively), which also represents a shift from hole accumulation to electron accumulation at the material/metal contact. There is a critical point where the bands are flat across the metal/semiconductor interface, known as the flat-band voltage V_{FB} (purple square in Fig.3.4 (a)) and it is found to be -1.1 V. Notably, this point marks the end of hole tunneling and the beginning of electron tunneling [82]. In some unipolar devices, the minority current is usually neglected, so V_{FB} is considered the critical point for turning on or turning off the tunneling current.

When focusing only on the n-branch/electron current $I_{electron}$ from -1.1 V to 10 V

(Fig.3.4 (c)), at low V_{GS} below V_{FB} at -1.1eV, electrons are only injected through thermionic emission from source over the barrier and no tunneling effect contribute to the I_{electron}, as a slightly larger gate voltage is applied ($V_{\mathrm{FB}} < V_{\mathrm{GS}} < V_{\mathrm{th,n}}$, $V_{\mathrm{th,n}}$ = -0.8 V), the device is at a sub-threshold regime, a triangular shaped-barrier region forms at the metal/MoS_2 interface near the conduction band. Here, I_{electron} is a combination of thermionic emission and tunneling currents. As the V_{GS} surpasses the $V_{\mathrm{th,n}}$, the tunneling component gradually becomes dominant in the I_{electron}. This transition is attributed to, on one hand, the barrier height for thermal emission remains constant in this region, whereas, on the other hand, the tunneling barrier becomes narrower as V_{GS} increases. At V_{GS} = 10 V, the tunneling current becomes 10 times larger compared to the thermal emission current. The same principle also works for hole current I_{hole} behavior.

3.4 Contact Area-Dependent Electron Transport in MoS_2 SBFETs

Edge contact is applied in the simulation, meaning that the metal contacts MoS_2 through the side [83]. Due to the atomic-scale thickness of MoS_2, the contact area between MoS_2 and metal always depends on the thickness of MoS_2. Given that the thickness of MoS_2 is always less than that of the metal, a uniform depletion layer forms at the interface if the contact is Schottky type. Next, we examine the effect of the contact area by varying the thickness of MoS_2 from 5 nm to 200 nm. It is important to note that the thickness of metal is fixed at 50 nm. When the thickness of MoS_2 surpasses that of the metal, MoS_2 devices begin to resemble conventional Si-based devices more closely. Although the electrical parameters of MoS_2 are thickness-dependent, to control the variables, only the thickness itself is changed during this series of simulations, excluding other parameters.

A contact area-dependent study is first performed for the Ohmic contact case. Our simulation results indicate that for Ohmic contact, the current is proportional to the contact area as shown in Fig.3.5(a). This can be understood as the resistance of the semiconductor being inversely proportional to the cross-sectional area. Therefore, after normalization, the current density $J = I_{\mathrm{DS}}/S_{\mathrm{MoS_2}}$ remains constant at around 320 A/cm^2, as shown in Fig.3.5(c), only slight degradation in current density is observed when the MoS_2 thickness exceeds that of the metal (t_{MoS_2} = 100 nm and 200 nm). The Ohmic contact shows good consistency in current density with height variation, which is speculated to be attributed to the uniform distribution of charge carriers, as shown in Fig.3.5(e). It is concluded that even metal contacts with small size can collect all carriers from semiconductors bulk through an Ohmic contact.

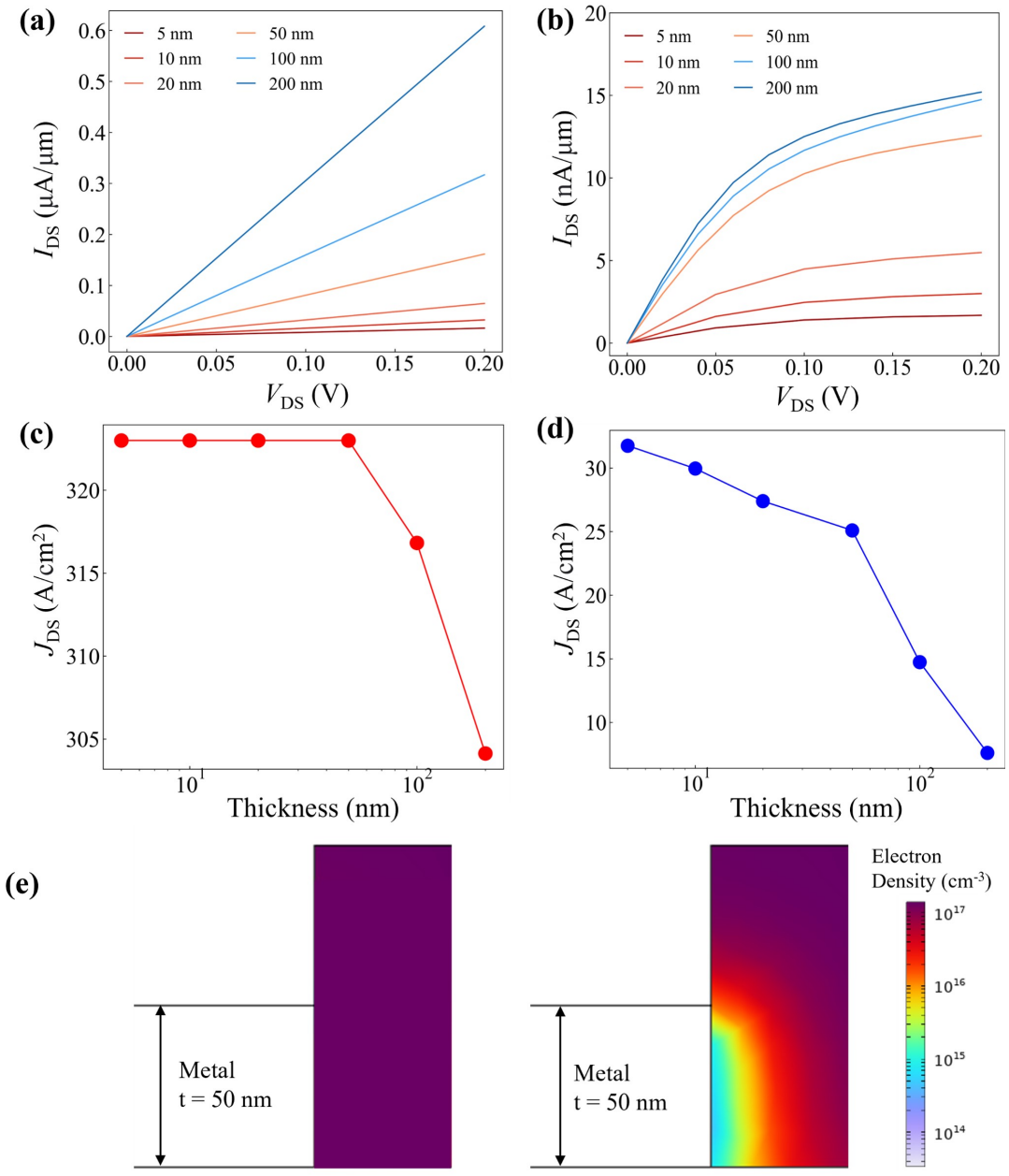

Figure 3.5: Thickness-dependent output characteristics of MoS_2 FETs with Ohmic contacts (a), Schottky contacts (b), $V_{GS} = 0$ V, $\Phi_{B,n} = 0.3$ eV. Current density J versus different thickness of MoS_2 at $V_{DS} = 0.2$ V, Ohmic contacts case (c), Schottky contacts case (d). Electron density distribution near the metal/MoS_2 contacts, Ohmic contacts case (e), Schottky contacts case (f), $V_{DS} = 0.2$ V.

In contrast, for Schottky contact, the current also shows linearity to the cross-sectional area when the thickness of MoS_2 is less than that of the metal ($t_{MoS_2} < 50$ nm). However, as the thickness of MoS_2 becomes greater than that of the metal ($t_{MoS_2} > 50$ nm), the growth rate of current versus thickness slows down significantly and the linearity no longer exists as shown in Fig.3.5(b). It is anticipated that the current will reach a maximum as the thickness continues to increase. Correspondingly, as shown in Fig.3.5(d), the current density initially drops slowly but remains stable in general, then decreases rapidly as the thickness of MoS_2 exceeds that of the metal. Fig.3.5(f) shows that the distribution of electrons is non-uniform at the interface. This non-uniformity is speculated to induce a current crowding effect [84], which always occurs near the edge of the contact points. This phenomenon is particularly evident when the metal contact area is significantly smaller than the cross-sectional area of the semiconductor [85], the current must converge to flow through the small contact. Compared to Ohmic contact, the existence of a depletion region at the contact interface further exacerbates this effect. This effect is speculated to hinder the current flow through the metal interfaces of the devices.

3.5 MoS_2 SBFETs with Schottky Barrier Height across Bandgap

In our next investigation, we examine the impact of metal-MoS_2 contact on the electrical transport characteristics using the MoS_2 FET model using the MoS_2 SBFET model validated in Sec.3.2, We explore a broad spectrum of Φ_m ranging from 4.0 eV to 5.3 eV, which covers most typical metals utilized for contacts to MoS_2. This range corresponds to the bandgap energy 1.3 eV of the multilayer MoS_2, whose electron affinity is 4 eV. It is worth noting that consistent mobility is assumed to be 25 $cm^2V^{-1}s^{-1}$ [26] for both electrons and holes in MoS_2, irrespective of the metal employed. First, we plot quasi-electron and hole Fermi levels ($E_{F,p}, E_{F,n}$) near the metal/semiconductor contact for different Φ_m and V_{GS} in Fig.3.6. It can be seen that the doping concentration near the contact interface highly depends on Φ_m. It also illustrates the trend of gate voltage regulation effect, which slows down significantly as the absolute value of gate voltage gradually increases, ultimately reaching saturation. In addition, $E_{F,p}, E_{F,n}$ almost align with the valence band and the conduction band when Φ_m of < 4.2 eV or > 5.2 eV, respectively, indicating that ohmic contacts are formed,

Fig.3.7 illustrates two opposite-polarity conducting regimes. With Φ_m sweeping from 4.0 eV to 4.6 eV with the step of 0.2 eV (Fig.3.7 (a)). A significant reduction in current is observed with an increasing Φ_m, owing to the higher $\Phi_{B,n}$ as the Fermi level of metals

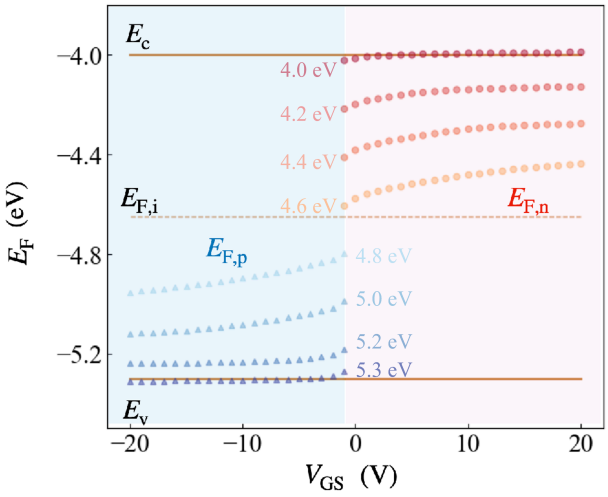

Figure 3.6: Quasi-Fermi level positions as a function of applied gate voltages for metal contact with different Φ_m, quasi-electron for Φ_m of 4.0 - 4.6 eV, and quasi-hole for Φ_m of 4.8 - 5.3 eV.

moves further away from the conduction band. For larger Φ_m (> 4.6 eV) metals, lower $\Phi_{B,p}$ leads to the p-type FET transfer characteristic (Fig.3.7(b)). The results imply that for the natural n-doped MoS_2 multilayers, either p- or n-type FETs can be built by selecting metals with appropriate Φ_m values concerning E_F as shown in Fig.3.7(c). However, practical MoS_2 FETs behave primarily as n-type transistors and rarely as p-type transistors. We attribute this to the strong FLP near the conduction band of MoS_2. Given the pinned Fermi level alignment, the relatively large $\Phi_{B,p}$ hinder hole injection. In addition, SBFETs are expected to function as ambipolar transistors via gating effect [86] in principle. In such transistors, a positive V_{DS} drives electrons from the source to the drain while simultaneously driving holes in the opposite direction. A typical example is the black phosphorus (BP) transistor [87]. However, our simulation shows that MoS_2 lacks this capability. It's challenging to achieve comparable currents from both the p-branch and n-branch. This limitation can be attributed to the relatively large band gap of multilayer MoS_2 [86] (1.3 eV compared to BP's 0.4 eV) and FLP, Interestingly, BP is found not to suffer from FLP [88]. It is reasonable to speculate that a weak ambipolar situation occurs around work function 4.7 eV, which is located at the midpoint of the bandgap, leading to identical barrier height for electrons and holes, however, the corresponding current level is too small for practical utility.

Next, the on/off ratio with respect to Φ_m, calculated by taking the ratio of the maximum

to the minimum I_{DS} values from Fig. 3.7(a) and (b) for p- and n-type regimes, is depicted in Fig. 3.7(d), This ratio decreases as the device transitions from unipolar n-type conduction to ambipolar conduction, reaching a minimum of 3×10^3 at $\Phi_m = 4.6$ eV. As Φ_m increases further into the p-type conduction region, the on/off ratio rises again, returning to the high levels seen in the n-type region. Specifically, it shows a high on/off ratio of around 3×10^{14} at Φ_m values of 4.2 eV and 5.2 eV.

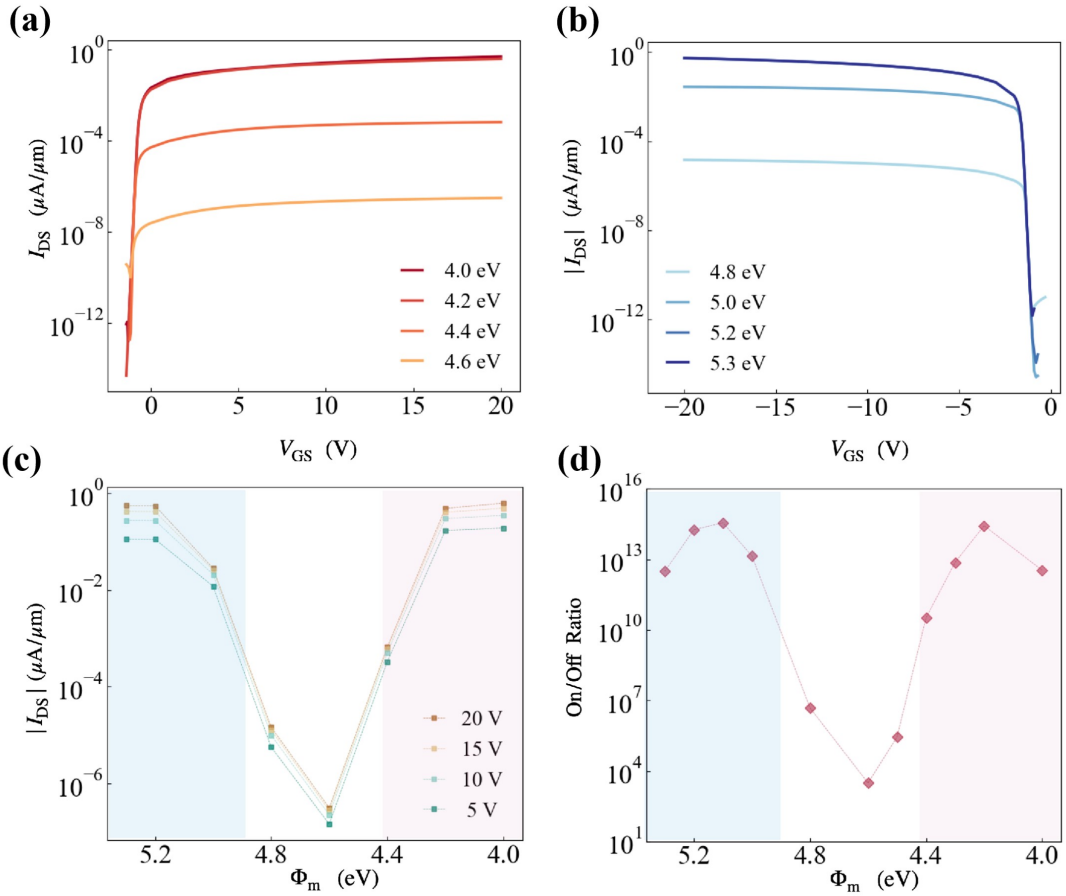

Figure 3.7: The effect of various metal contacts with a wide range of Φ_m on multilayer MoS_2 SBFETs. Transfer characteristics of p-type FETs (a) or n-type FETs (b) for metals with different Φ_m at $V_{DS} = 0.2$ V. (c) I_{DS} as a function of Φ_m of applied contact metals at different V_{GS}. (d) On/off ratio as a function of Φ_m of applied contact metals.

The Φ_m-tunability trend of the on/off ratio is explained by the I_{on} values because a

larger $\Phi_{B,n}$ ($\Phi_{B,p}$) hinders the transport of electrons (hole). On the other hand, I_{off} exhibits an opposite trend to the on/off ratio against Φ_m, peaking near the midpoint of Φ_m where the Schottky barrier heights are roughly equal, $\Phi_{B,n} \approx \Phi_{B,p}$.

Lastly, we consider the behavior of V_{th} and V_{FB} in terms of metal choices. V_{th} is found to be generally independent of metal choice, V_{th} for holes ($V_{th,p}$) of -2 V and electrons ($V_{th,n}$) of -0.8 V is consistently observed across various Φ_m from Fig.3.7(a) and (b), it's worth noting that gap between $V_{th,p}$ and $V_{th,n}$ closely matches band gap of multilayer MoS_2 (1.3 eV). Regarding V_{FB}, V_{FB} at four V_{DS} cases exhibit a decreasing trend as Φ_m increases. Here we omit the discussion of the physical interpretation of the V_{FB} and V_{th}, the V_{th} corresponds to the point at which the conduction band edge coincides with the metal Fermi level while flat band voltage corresponds to the points at which conduction band bending is canceled under the gate modulation. With the elevated $\Phi_{B,n}$ due to the increased work function, the gate voltage range between V_{FB} and $V_{th,n}$ must also expand to accommodate this change. Since $V_{th,n}$ is independent of barrier height, so flat band voltage has to consequently occur the further away $V_{th,n}$ the larger $\Phi_{B,n}$ [76].

3.6 Ambipolar MoS_2 SBFETs with Asymmetric Electrode Metals

Based on the study of the metal Φ_m effect on the device polarity in Sec.3.6, a MoS_2 SBFET with different metals for the source and drain electrodes is simulated to enable ambipolar characteristics. Specifically, Pd with a $\Phi_{B,p}$ of 0.45 eV [65] is selected for the drain electrode to facilitate hole injection, while Au with a $\Phi_{B,n}$ of 0.45 eV [70] is chosen for the source electrode to supply electrons. Au is used because it is one of the most commonly used and stable metals for contact with 2D materials, Pd is chosen because it is one of the few metals capable of forming *p*-type contacts with MoS_2. Our study is complemented by comparing the results obtained with symmetric SBFETs whose both the S and D are composed of either Au or Pd. The Au-Au device functions as a unipolar *n*-SBFET, with current flow occurring at positive V_{GS} while the Pd-Pd device operates as a unipolar *p*-SBFET, with current flow at negative V_{GS}. In contrast, as illustrated in Fig.3.8(a), the Au-Pd configuration exhibits ambipolar characteristics, allowing for current flow in both *n*-type and *p*-type regimes.

When no bias is applied (V_{GS} = 0 V, V_{DS} = 0 V), the E_F of Pd aligns closely with the valence band of MoS_2 to form a *p*-type contact, while E_F of Au near the conduction band induces a *n*-type contact as shown in Fig.3.8 (c). For a fixed V_{DS} = 1 V, applying

a positive V_{GS} facilitates thermionic electrons movement over a reduced Schottky barrier, dropping from 0.45 eV to 0.3 eV at the left electrode, Then the curvature of the band at the contact interface also increases and the Schottky barrier region becomes thinner, leading to a larger tunneling current. A representative band diagram of n-type transport at $V_{GS} = 10$ V is illustrated in Fig.3.8(d) (top box). Conversely, upon applying a negative V_{GS} of -10 V, the band bending curvature is reversed to be upwards for hole-dominated transport from both thermionic and tunneling processes (bottom box). Similarly, Both thermionic and tunneling hole currents experience enhancement through the right side, where the situation is just the opposite of the positive V_{GS} case.

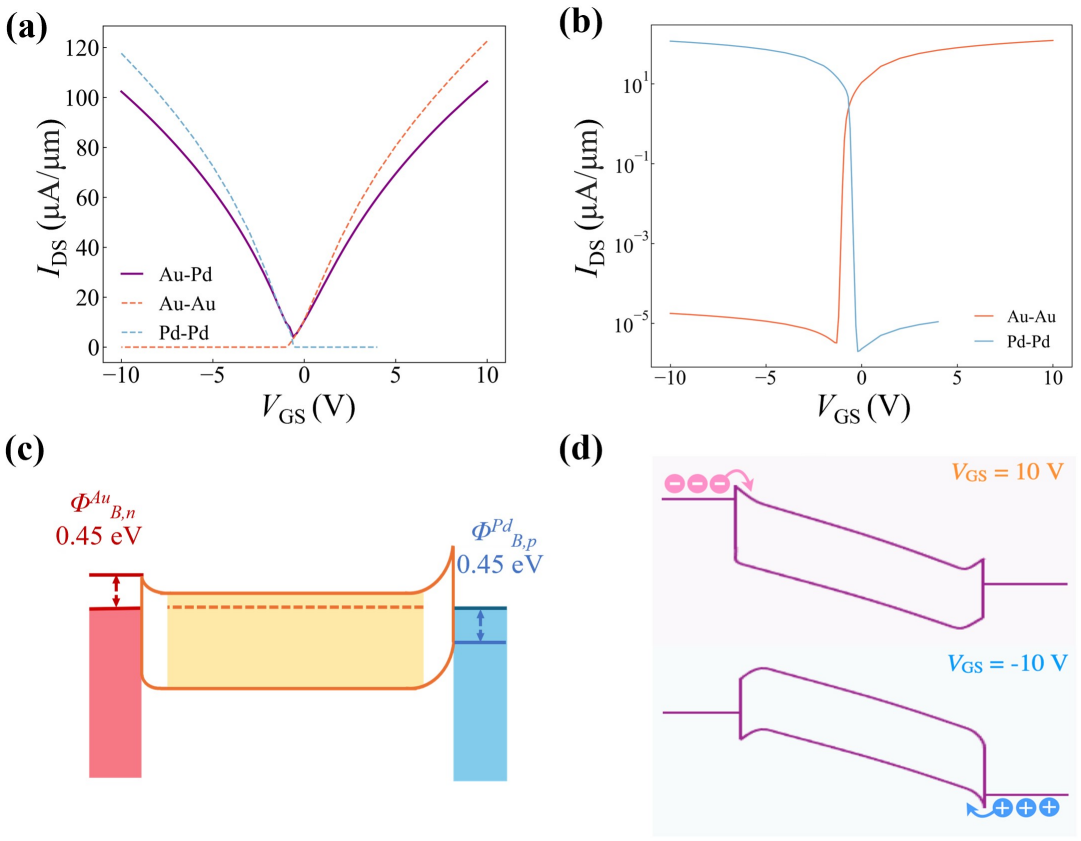

Figure 3.8: Multilayer MoS_2 SBFETs with asymmetric metal electrodes of Au (source) and Pd (drain). (a) Transfer characteristic for MoS_2 SBFETs with asymmetric metals and with symmetric metals, which are biased at $V_{DS} = 1$ V. (b) Corresponding energy band diagrams of MoS_2 SBFETs with asymmetric metals from (a) at $V_{GS} = \pm 10$ V.

Fig.3.8(b) illustrates the V_{GS}-I_{DS} for devices with symmetric Au-Au and Pd-Pd contacts on a logarithmic scale, Both devices exhibit a similar on/off ratio in the order of 10^7. The comparison between the transfer characteristics of asymmetric and symmetric MoS_2 SBFETs reveals that the on-state current magnitude in asymmetric SBFETs is comparable to those in symmetric SBFETs employing either metals as contacts. However, for devices with Au-Pd contacts, the off-state current is significantly increased, resulting in a reduced on/off ratio as low as 10^2. This can be attributed to ambi-conduction within the original subthreshold region, between $V_{th,p}$ (-2 V) and $V_{th,n}$ (-0.8 V). The combined currents from the electron and hole branches determine the I_{min}.

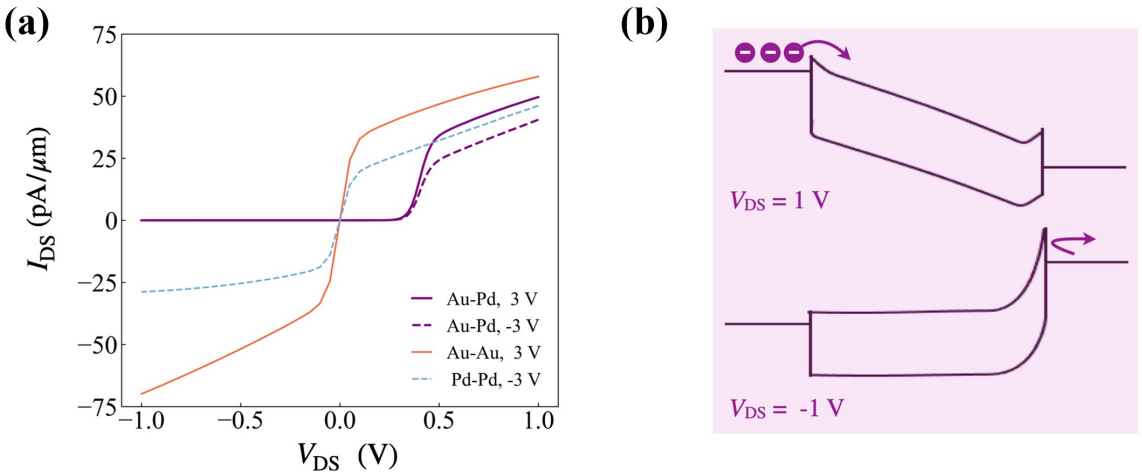

Figure 3.9: Multilayer MoS_2 SBFETs with asymmetric metal electrodes of Au (source) and Pd (drain). (a) Output characteristics for MoS_2 SBFETs with asymmetric metals and with symmetric metals at $V_{GS} = \pm 3$ V. (b) Energy band diagrams of MoS_2 SBFETs with asymmetric metals from (a) at $V_{DS} = 1$ V (top) and -1 V (bottom) under the same $V_{GS} = 3$ V.

The I_{DS} - V_{DS} characteristics of the simulated device are shown in Fig.3.9(a). With positive V_{DS} of 1 V (Fig.3.9(b), top), The asymmetric device shows a current flow of similar magnitude to that of the symmetric device, and the current under opposite polarity of gate bias (V_{GS} = 1 V and V_{GS} = -1 V) are also comparable, This suggests that similar resistances are obtained when the simulated device operates in both the n-type and p-type regions. However, when V_{DS} = -1 V (Fig.3.9(b), bottom), a large Schottky barrier of 0.8 eV increased from 0.45 eV formed at the right side ($V_{GS} > 0$ V) or the left side ($V_{GS} < 0$ V), leading to significantly reduced current levels and resulting in rectifying behavior. A

rectification ratio (RR) is calculated from the ratio of the forward and reverse currents measured at the same magnitude of $\pm V_{\mathrm{DS}}$. While reported RR values of MoS_2 SBFETs are $10^3 - 10^4$ [58], the estimated RR values at $V_{\mathrm{DS}} = \pm 1$ V from the device are 4×10^6 at $V_{\mathrm{GS}} = 3$ V and $8{\times}10^6$ at $V_{\mathrm{GS}} = -3$ V. Thus, the simulated device shows potential as both an ambipolar device and a Schottky rectifying diode.

Chapter 4

Electrical and Optical Performance Simulation of Dual-gated MoS_2 FETs

It was demonstrated in Chapter 3 that having one terminal facilitate electron transport while the other facilitates hole transport is crucial for achieving ambipolar conduction. This requirement is also important for high-performance photodiodes, where efficient collection of electrons and holes at different terminals is expected. Therefore, this chapter focuses on studying the electrical and optical performance of a dual-gated MoS_2 photodiode. This photodiode is based on the FET with asymmetric metals introduced in Chapter 3.6, with the new dual gates design enabling it to function as a photodiode.

4.1 Modeling Setup and Parameter

The built-in voltage at a $p-n$ junction is fundamental for establishing a photodiode. Numerous studies [54, 55, 56, 53] have reported the formation of the hetero $p-n$ junction between MoS_2 and other 2D materials, the fabrication techniques can be broadly categorized into mechanical transfer and CVD growth [1]. However, an intrinsic problem in both processes is that the formation of heterostructure is always accompanied by interface quality, reliability, and stability issues. These problems arise due to the atomic thickness of MoS_2, significantly degrading device performance. Therefore, People seek other methods to fabricate homogeneous $p-n$ junctions within single MoS_2 materials, such as chemical doping by plasma treatment [89], appropriate voltage drop between drain and source relative to an ionic gate [90].

Here, MoS_2 FETs feature dual back gates to achieve a controllable and reconfigurable homogeneous $p-n$ junction in MoS_2 are assessed by simulation, in which dual gates perform independent spatial control of a channel [91, 92, 93]. Fig.4.1(a) sketches the schematic of a dual-gate asymmetric MoS_2 SBFET, and relevant new parameters for this simulation are listed in Table.4.1. To accurately model the behavior of leakage current under reversed bias The Shockley-Read-Hall recombination is introduced to this model in terms of lifetimes for electrons (τ_{n}) and holes (τ_{p}).

Unlike the conventional FET, in this device, the drain contact and half channel are covered by the control gate (CG) while the source contact and the other half channel are covered by the program gate (PG) [94]. This configuration enables independent electrostatic control on the local doping of the right and left sides of the channel, along with the adjustment of the local Schottky barrier height [95]. By applying opposite or identical voltages to two gates, the device demonstrates diverse functionality.

Table 4.1: MoS_2 dual-gated FETs design parameters. All the data are taken from Ref. [66], † [21], ‡ [26], § [81].

Parameters	**Value**	**Parameters**	**Value**
$t_{\mathrm{MoS_2}}$ (nm)	10	m_h^*	0.5 $m_0^{\dagger}$
$L_{\mathrm{MoS_2}}$ (nm)	5000	m_e^*	0.5 $m_0^{\dagger}$
$W_{\mathrm{MoS_2}}$ (nm)	1000	N_{c} (m^{-3})	8.57×10^{24}
t_{metal} (nm)	50	N_{v} (m^{-3})	8.57×10^{24}
$t_{\mathrm{SiO_2}}$ (nm)	100	N_{D} (m^{-3})	1.4×10^{23}
t_{Si} (nm)	2000	μ ($\mathrm{cm}^2/(\mathrm{V}\cdot\mathrm{s})$)	25‡
T (K)	293.5	$A^*_{n(p)}(\mathrm{A}/(\mathrm{K}\cdot\mathrm{cm})^2)$	60
E_g (eV)	1.3§	$\epsilon_r(\mathrm{MoS_2})$	11†
$\chi_{\mathrm{MoS_2}}$ (eV)	4‡	Contact type	Ideal Schottky
L_{CG} (nm)	3000	L_{PG} (nm)	3000
Drain $\Phi_{\mathrm{m,F}}$ (eV)	4.85	Source $\Phi_{\mathrm{m,F}}$ (eV)	4.45
τ_{n} (ns)	0.1‡	τ_{p} (ns)	0.1‡

4.2 Electrical Performance Simulation of Dual-gated MoS_2 FETs

4.2.1 Reconfigurable Functionality through Gate Voltage Control

There are four distinct conducting regions determined by the polarity of the gate bias applied to the dual gates, as depicted by corresponding I_{DS} - V_{DS} in Fig.4.1. When equal bias is applied to both gates ($V_{\mathrm{GS}} = V_{\mathrm{CG}} = V_{\mathrm{PG}}$), the device functions as a single global gate device, identical to the FET with asymmetric metals described in Section 3.6. If both sides are positively gating biased ($V_{\mathrm{GS}} > 0$ V) or negatively gating biased ($V_{\mathrm{GS}} < 0$ V), the entire MoS_2 channel becomes either purely n-doped or p-doped, labeled NN or PP, respectively. On the other hand, applying opposite-polarity biases to the gates ($V_{\mathrm{G}}S = V_{\mathrm{PG}} = -V_{\mathrm{CG}}$) turns the device into a $p - n$ MoS_2 heterostructure (denoted PN or NP), where spatial electrostatic gating efficiently modifies local doping type and concentration. The $I_{\mathrm{D}}S$ - V_{DS} characteristics for these four configurations, presented in Fig. 4.1(b), demonstrate clear rectifying behavior.

For NN and PP configurations, rectification originates from the asymmetric metal configuration and Schottky barrier as discussed in Sec 3.6. The RR is measured at $8{\times}10^6$ for PP and $4{\times}10^6$ NN, The I_{DS} - V_{DS} behavior for PN and NP configuration is fitted to the Shockley diode equation with series resistance (R_s) taken into account [79].

$$I_{\mathrm{DS}} = I_0(e^{(V_{\mathrm{DS}} - I_{\mathrm{DS}}R_s)/\eta V_{\mathrm{T}}} - 1) \tag{4.1}$$

where I_0 is the reverse saturation current, R_{S} is the series resistance, η is the diode ideality factor, V_{T} is the thermal voltage. By fitting Fig.4.1(c) and Fig.4.1(d) to this equation, the part of the $I_{\mathrm{D}}S$ - V_{DS} where the current increases exponentially with forward bias specifies a $\eta = 1.7$ for PN configuration and $\eta = 1.8$ for NP configuration. The deviation of both values from the ideal case ($\eta = 1$) should be attributed to the presence of the Shockley–Read–Hall recombination process. As V_{DS} increases, the current becomes linear with forward bias, and the fits in this linear region yield $R_{\mathrm{s}} = 8$ BΩ for PN and 100 TΩ for NP configurations. This significant resistance is due to the presence of the Schottky barrier.

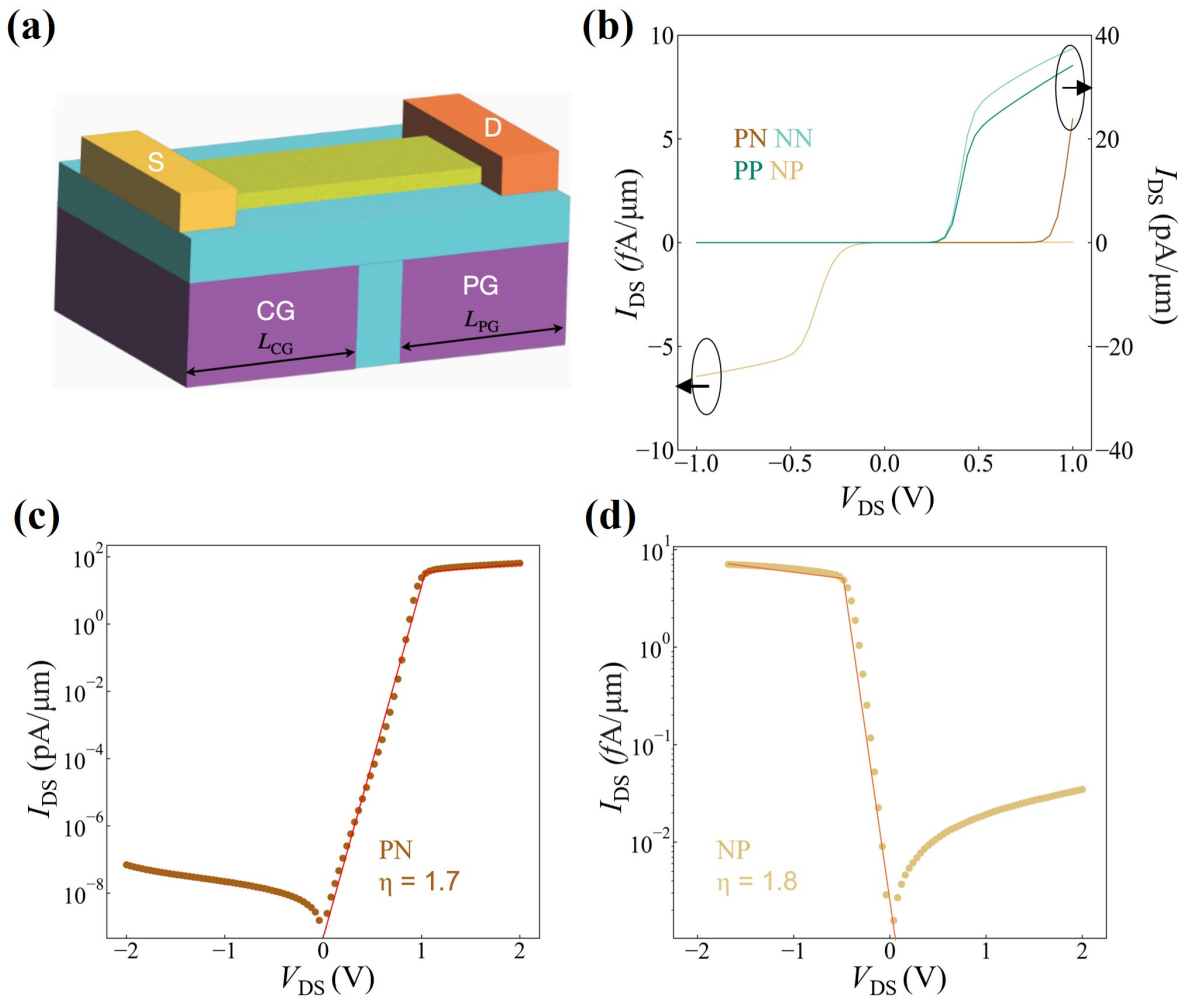

Figure 4.1: Dual-gated MoS_2 SBFETs with asymmetric electrode metals (a) Illustration of the dual-gate MoS_2 SBFET device with control gate (CG) and program gate (PG) at the bottom (b) $I_{DS}-V_{DS}$ curves showing transport characteristics of four various configurations of the device: NN, PP, PN and NP. Both gate voltages are set to be 3 V for NN and –3 V for PP. V_{CG} = 3 V for NP and -3 V for PN. (c) Semi-logarithmic plots of $I_{DS} - V_{DS}$ for PN configuration, with fits in red. The fits give a diode ideality factor η of 1.7 and series resistance R_s of 8 BΩ (d) Semi-logarithmic plots of $I_{DS} - V_{DS}$ for NP configuration, with fits in orange. The fits give a diode ideality factor η of 1.8 and series resistance R_s of 100 TΩ.

The role of the Schottky barrier is crucial in this device, offering both advantages and disadvantages. On the negative side, the asymmetric contact resistance (8 BΩ for PN and 100 TΩ for NP) leads to I_{DS} - V_{DS} that are not mirror images for the PN and NP configuration. Specifically, the negligible current observed in NP is due to the extremely high R_s, which should be attributed to the metal configuration: Au for hole transport and Pd for electron transport, relatively large Φ_{B} are formed at both contacts as a consequence. On the other hand, the outstanding rectifying properties observed in the PN configuration are enhanced by the Schottky barrier, the contribution of the Schottky barrier can be found in the I_{DS} - V_{DS} of NN and PP configurations in Fig.4.1(b), where no potential barrier exists within the MoS_2.

4.2.2 Study of Diode Behavior in PN Configuration

Next, we focus on the PN configuration only, where $V_{\mathrm{CG}} = -V_{\mathrm{PG}} = V_{\mathrm{GS}}$. The potential barrier (Φ_{p}) and the depletion region of this $p-n$ junction are modulated by the gate bias, as shown in Fig.4.2 (a). A higher V_{GS} results in increased doping concentration, leading to a narrower depletion region width and a larger Φ_{p} compared to a lower V_{GS} case. A rapid increase in Φ_{p} is observed as V_{GS} varies from 1 V to 3 V, after which Φ_{p} remains nearly constant from 3 V to 5 V. This suggests that the gating-induced doping has reached saturation around $V_{\mathrm{GS}} = 3$ V. Changes in the heterojunction further induce corresponding changes in the I_{DS} - V_{DS} characteristics, the rectifying behavior at various V_{GS} is illustrated in Fig.4.2 (b) and (c) shows the output characteristics in linear and logarithmic scales, respectively.

Both forward currents (I_{f}) and reverse currents (I_{r}) are effectively modulated by gate bias but exhibit the opposite dependencies: I_{f} increases as V_{GS} increases from 1 V to 5 V while I_{r} decreases with increasing V_{GS}. This phenomenon enhances the RR, which changes from 6.5×10^6 at $V_{\mathrm{G}} = 1$ V to 3×10^9 at $V_{\mathrm{G}} = 5$ V (Fig.4.2(d)), corresponding to a 450-fold enhancement. The monotonic trend of RR versus V_{GS} can be attributed to the simultaneous presence of the Schottky junction at the contact and the $p-n$ junction in the middle of this device. The competition between these junctions results in varied current transport mechanisms across different bias regimes.

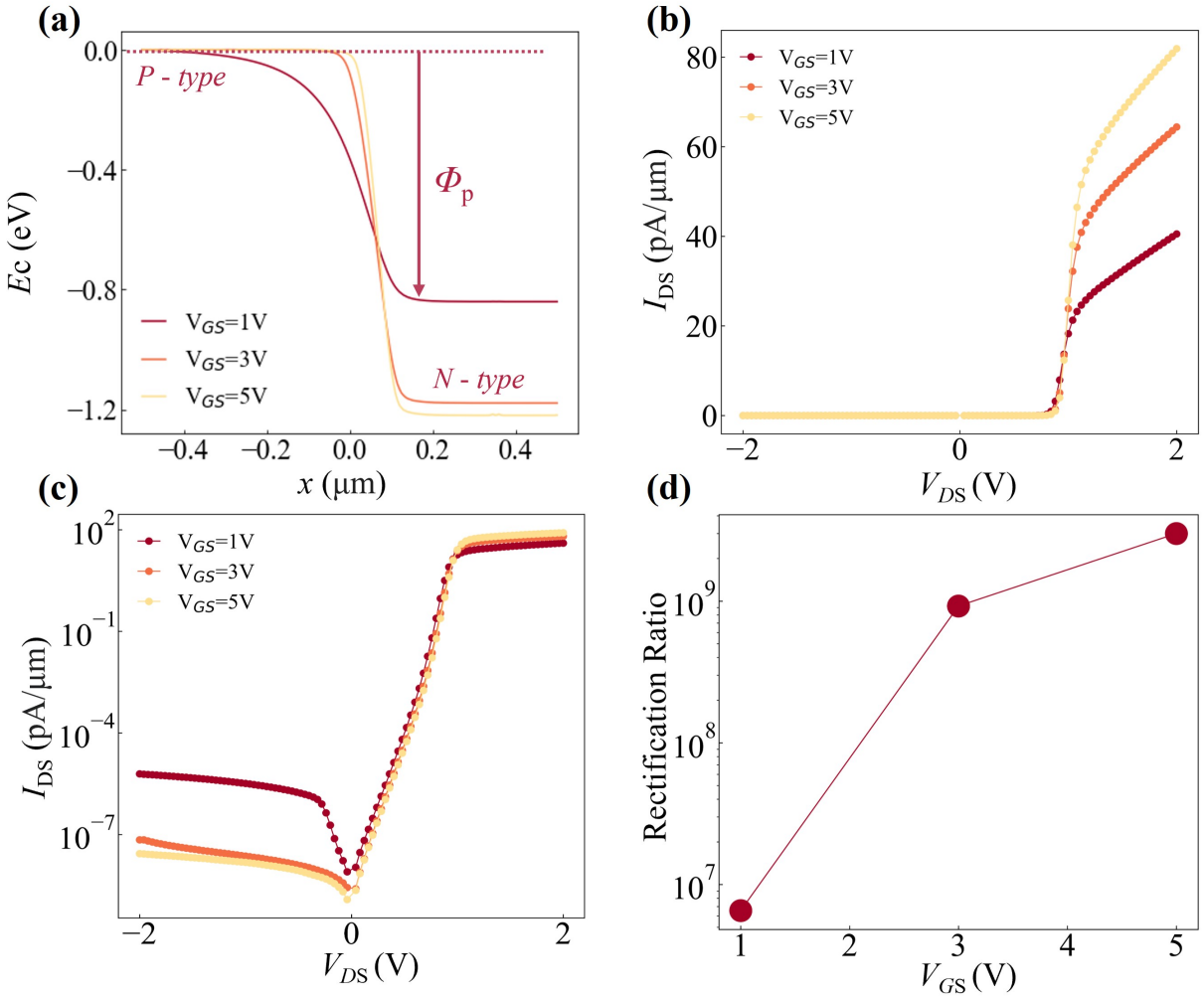

Figure 4.2: Gate voltage V_{CG} dependence of transport properties in dual-gated MoS_2 SBFETs. (a) Linear scale plot of $I_{DS} - V_{DS}$ characteristics of the $p - n$ MoS_2 dual-gate SBFET at three different V_{GS} values. Particularly, the opposite bias is applied to the CG and PG gates in $V_{CG} = -V_{PG} = V_{GS}$. (b) Logarithmic scale pot of the $I_{DS} - V_{DS}$. (c) Conduction band (E_c) profile across the $p - n$ junction region at various V_{GS} and V_{DS} = 0 V, E_c at p-type MoS_2 body (region far from the junction) is positioned at 0 eV. Barrier potential (Φ_p) is labeled as the distance between the E_c of p-type and n-type MoS_2. (d) Rectification ratio of dual-gated MoS_2 SBFETs as a function of V_{GS}.

When the device is reverse biased ($V_{DS} < 0$ V), current transport is primarily dominated by the p−n junction as the Schottky barrier becomes negligible compared to that of the p−n junction, as illustrated in Fig.4.3(a). This indicates that reversed currents originate mainly from the diffusion of minority carriers and they are inversely proportional to the doping concentration in the p- and n- region. Therefore, the enhancement of doping concentration by gate voltages effectively suppressed I_0 as V_{GS} changes from 1 V to 3 V as shown in Fig.4.2 (c). This trend correlates with the rapid increase in Φ_p observed in Fig.4.2 (a) when V_{GS} changes from 1 V to 3 V. Both observations indicate that V_{GS} has a significant tuning capability for the $p-n$ junction when V_{GS} is less than 3 V.

On the other hand, in the forward bias regime ($V_{DS} > 0$ V), the I_{DS} - V_{DS} characteristic does not follow the Shockley diode relation (Equation 4.1), where the current I is expected to be exponentially related to I_0 so a larger I_0 should correspond to a larger I_{DS}. However, as shown in Fig.4.2(c), the observation shows that a larger I_0 corresponds to a smaller I_{DS}. This behavior can be attributed to that the Schottky junction replaces the dominant position of $p-n$ junction in this regime (Fig.4.3(b)). As a larger V_{GS} is applied, $\Phi_{B,p}$ at the right electrode and $\Phi_{B,n}$ at the left electrode decrease simultaneously. This reduction in $\Phi_{B,n(p)}$ facilitates the carrier transport, resulting in a higher forward bias current. Simulation results suggest that optimized RR can be achieved by dual-gate biases as another control parameter.

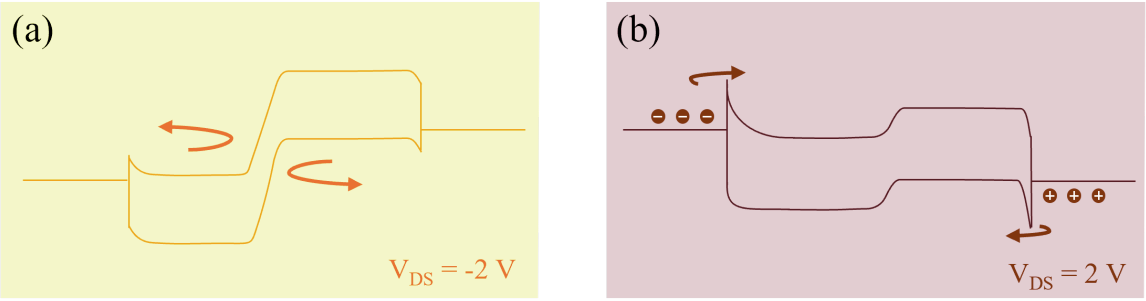

Figure 4.3: Band diagrams of the negative V_{DS} (a) and the positive V_{DS} (b) to explain the rectifying behavior.

4.3 Optoelectronic Performance Simulation of Dual-gated MoS_2 FETs

4.3.1 Model Setup and Parameters

In Sec.4.2, we present the simulation model of dual-gated MoS_2 SBFETs, highlighting its ability to establish a $p-n$ junction by electrostatic gating. The resulting built-in voltage facilitates the separation of photogenerated electron-hole pairs. Therefore, it has the potential in the application of photodiode. The photocurrent originates from the absorption of light, which generates electron-hole pairs. These pairs are then collected by opposing electrodes to generate current, facilitated by an electric field that separates and directs electrons and holes in opposite directions. In this section, we characterize its optoelectronic properties by analyzing some important parameters.

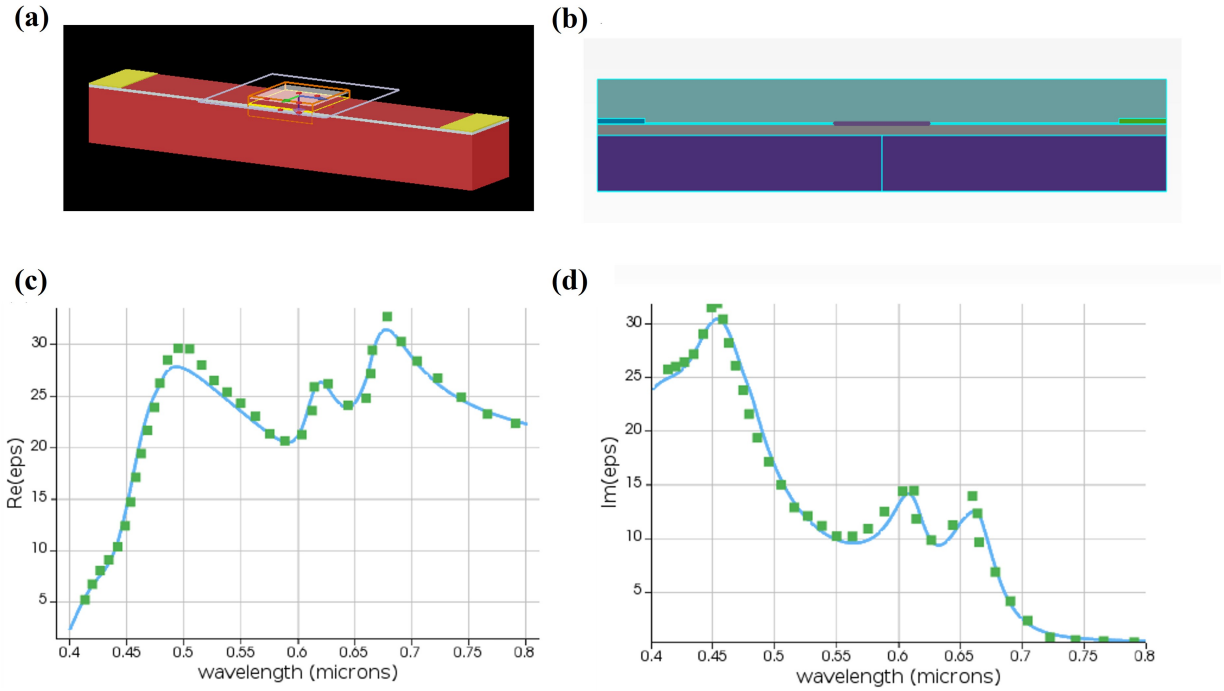

Figure 4.4: Schematic diagram of the FDTD(a) and CHARGE(b) model of a dual-gated MoS_2 FETs model. Real part(c) and imaginary part(d) of the dielectric function of multilayer MoS_2 in the visible region.

The simulation is conducted using Lumerical FDTD and CHARGE tools by applying the scheme introduced in Sec.2.4.2. Specifically, for our simulation, the schematic diagram of the simulated device used in FDTD for optical absorption calculations is shown in Fig.4.4(a), while the schematic for photocurrent calculations using CHARGE is presented in Fig.4.4(b). In the FDTD simulations, multilayer MoS_2 is defined in terms of its dielectric function, with its parameters detailed in Figs.4.4(c) and 4.4(d).

4.3.2 Device Optoelectronic Characteristics

The photovoltaic effect of dual-gated MoS_2 SBFETs is then investigated. Here we only focus on PN ($V_{GS} > 0$ V) configuration and the bias region where the gain is produced, i.e., $V_{DS} < 0$ V. Simulation results in Fig.4.5(a) demonstrate the I_{DS} - V_{DS} characteristics under incident light across various power densities (P_{inc}) ranging from 0.01 to 5 mW/cm^2 at a wavelength of 532 nm. In addition, Fig.4.5(b) presents photocurrents ($I_{ph} = I - I_{dark}$) at -2 V as a function of power density. The linear response of photocurrent to the logarithmic change in optical power indicates a Responsivity, $R = I_{ph} / P_{in}$, calculated as 24.2 mA/W. This relatively low value can be attributed to the presence of the Schottky barrier and the direct band gap of MoS_2.

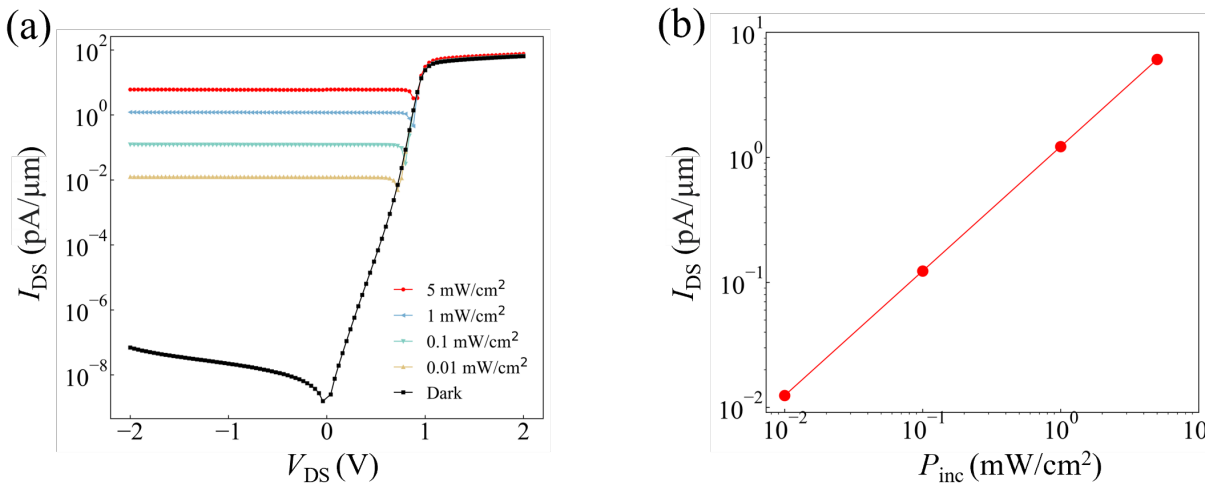

Figure 4.5: Optoelectronic behavior of dual-gated MoS_2 SBFETs. (a) Comparison of I_{DS} - V_{DS} under dark and light conditions with various incident optical power densities (λ = 532 nm, P_{inc} = 0.01, 0.1, 1, 5 mW/cm^2). (b) Responsivity as a function of incident power in logarithmic scale.

Given the coexistence of both the Schottky junction and $p-n$ junction in this device, it is necessary to distinguish their respective contributions to the photocurrent [91, 92]. To isolate the effect of the Schottky junction from the $p-n$ junction, we further segmented the simulation region to separately analyze the Schottky junction region. As shown in Fig.4.6(a), the top image shows the simulation of the entire channel material between the source and drain, including both the $p-n$ junction and Schottky junction areas, while the bottom image focuses only on the region near the metal contacts where the Schottky junctions form.

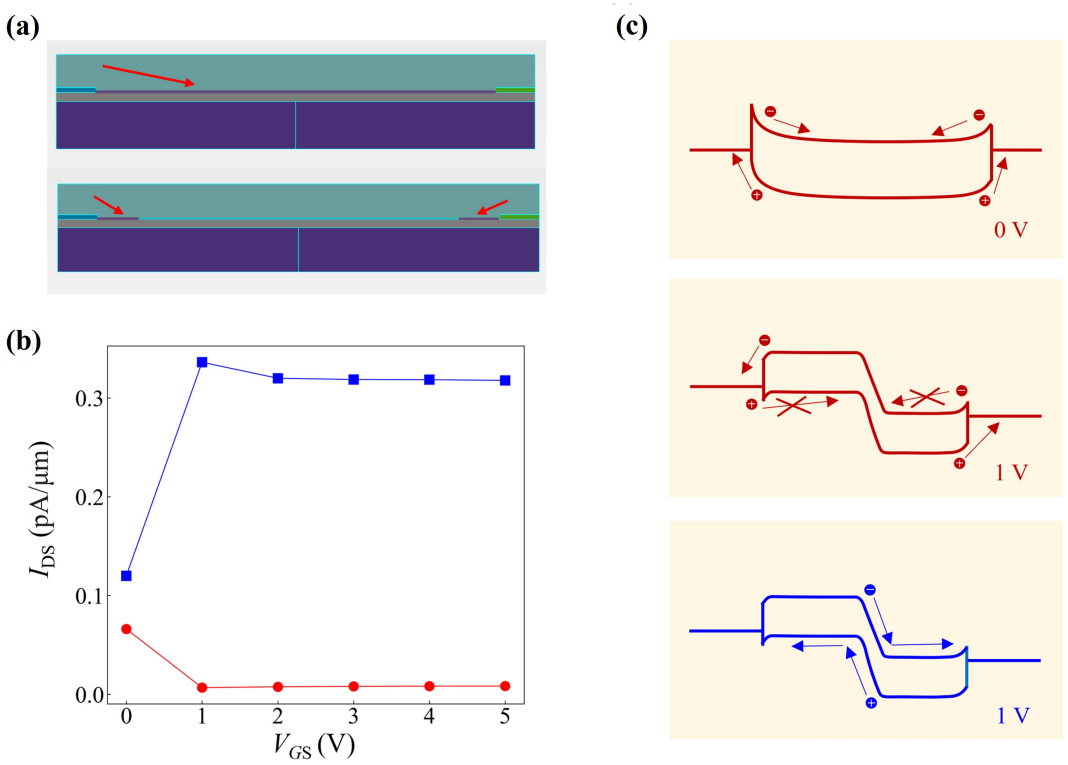

Figure 4.6: (a) Schematic diagrams of simulated devices in Lumerical CHARGE, showing two assumptions for the photogenerated region: entire channel material between Drain and Source (top, purple) and Schottky junction near Drain and Source (bottom, purple). (b) Overall Photocurrent (blue) and Schottky junction Photocurrent (red) as a function of different V_{GS}. (c) Band diagrams illustrating the behavior of the photogenerated carriers at different positions and conditions, top: metal contact and $V_{GS} = 0$ V, middle: metal contact and $V_{GS} = 1$ V, $p-n$ junction and $V_{GS} = 1$ V.

Since both the Schottky junction and $p-n$ junction are sensitive to V_{GS} in the simulated device, the photocurrents at different V_{GS} are plotted in Fig.4.6(b). The blue curve represents the overall photocurrent while the red curve represents the contribution specifically from the Schottky junction. When $V_{\mathrm{GS}} = 0$ V, no $p-n$ junction is created, making the Schottky junction the major contributor to the photocurrent. The corresponding band diagram is shown in Fig.4.6 (c) top, where the separation of photogenerated carriers is illustrated. The photocurrent originating from the source and drain should ideally cancel each other out, resulting in a net current that reflects the combined contribution of the two Schottky junctions. However, due to different Schottky barrier heights, the net current is non-zero. When $V_{\mathrm{GS}} > 0$ V, a $p-n$ junction is created at the center, and photocurrent generated at the Schottky junction is suppressed [96]. As shown in Fig.4.6(c) middle, the potential in the depletion region blocks one of the generated carriers. The current originating from the Schottky junctions is significantly reduced by 10 times as V_{GS} changes from 0 V to 1 V. In comparison, the $p-n$ junction becomes the primary source of photocurrent as shown in Fig.5.4(c) bottom, tripling the photocurrent as V_{GS} changes from 0 V to 1 V. In conclusion, the $p-n$ junction dominates the current flow in the PN configuration while the function of the Schottky junction is negligible.

In addition to separate electron-hole pairs. The Schottky barrier also yields additional contact resistance, which typically decreases the magnitude of the photocurrent generated by the $p-n$ junction, thereby adversely affecting device performance. A higher V_{GS} is expected to lower the Schottky barrier height, positively impacting the photocurrent. However, the highest photocurrent is observed at $V_{\mathrm{GS}} = 1$ V instead of the maximum examined V_{GS} of 5V, this phenomenon remains unexplained.

Chapter 5

Conclusion and prospects

5.1 Conclusion

This study presents a comprehensive device model for multilayer MoS_2-based SBFETs and analyzes their transport properties through simulation. our model are verified first with experimental data. Simulations results show that one of the key aspects to determine the electrical polarity of MoS_2 FETs in practice is correlated with the choice of metal electrodes. Even though MoS_2 FETs dominantly act as n-type transistors, p-type transistors can be indeed possible with high Φ_{m} metal electrodes and gate voltage control in the atmospheric environment. However, ambipolar conduction is still weak even when $\Phi_{\mathrm{B,n}} \approx \Phi_{\mathrm{B,p}}$. Therefore, we further extend this work for designing ambipolar MoS_2-based SBFETs by employing asymmetric metal contacts with Au-Pd as an example. The on-state performance of this configuration is comparable to symmetric MoS_2-based FETs, and the p-branch current behavior is also comparable to the n-branch one, which is promising to satisfy a critical requirement for CMOS logic circuits [97]. Our analysis shows that ambipolar conduction is achievable in any electrode configuration with one terminal being n-type and the other p-type.

In addition, We also investigate reconfigurable MoS_2 dual-gated FETs with Au - Pd contacts, where a heterojunction is realized in a single MoS_2 channel by electrostatic doping. The simulated device offers four distinct operating configurations: PP, NN, NP, and PN. However, perfect symmetric output characteristics are not obtained for NP and PN configurations due to significant contact resistance encountered in NP configuration. This proves the importance of appropriate metal configurations that facilitate efficient electron

and hole transport at the same time in such reconfigurable devices. Based on the potential of the above devices as photodetectors, we examine their optoelectronic performance.

The photoresponsivity of the simulated device is found to be 24.2 mA/W. Further study reveals that in this device, which features both Schottky junction and $p-n$ junction, the $p-n$ junction is always dominated in current transport. The change from $V_{\mathrm{GS}} = 0$ V to $V_{\mathrm{GS}} = 1$ V induces the formation of the $p-n$ junction, the thereby rapidly increased photocurrent proves that the $p-n$ junction is more efficient in separating electron-hole pairs compared to the Schottky junction.

It is worth noting that the proposed simulation is not only applicable to MoS_2, but also to any other material with known specific parameters. Therefore, the above simulation method has high universality.

5.2 Prospects

Compared to conventional doping methods used to create $p-n$ junction, this single-material heterojunction achieved by electrostatic doping is desirable to eliminate the complexities associated with the growth or deposition of a second material and to solve potential interface quality issues from dissimilar materials. In addition, For those devices doped through electrostatic gating, their operational modes can be flexibly tuned by adjusting gate voltages. However, to ensure comparable outputs for each working mode, careful consideration of the metal configuration is required. It is known that metals with work function close to the mid-band gap of the channel material band gap are generally suitable for facilitating both good electron and hole transport [91]. However, due to the Fermi pinning effect, the prediction of the actual Schottky barrier based solely on work function is less accurate. Therefore, additional studies of easy and practical methods on Fermi-level unpinning on MoS_2 will be needed to realize tunable Schottky barrier experimentally.

In addition, The drift-diffusion model, while highly effective in classical scenarios for describing the movement of charge carriers (electrons and holes), is typically used for traditional bulk semiconductors and long-channel devices [98]. It is well-suited for devices where quantum mechanical effects are negligible. However, it is less accurate for devices where quantum effects are significant, such as in very short channel lengths or low-dimensional materials like nanowires or 2D materials. As semiconductor technology advances and device dimensions continue to shrink to sustain Moore's Law, simulating devices must account for quantum effects in these cases, making the development and improvement of new methods imperative. Non-Equilibrium Green's Function [99] is a prominent example of such an approach.

Bibliography

[1] Suman Kumar Chakraborty, Baisali Kundu, Biswajeet Nayak, Saroj Prasad Dash, and Prasana Kumar Sahoo. Challenges and opportunities in 2D heterostructures for electronic and optoelectronic devices. *iScience*, 25(3):103942, March 2022.

[2] Max C. Lemme, Deji Akinwande, Cedric Huyghebaert, and Christoph Stampfer. 2D materials for future heterogeneous electronics. *Nature Communications*, 13(1):1392, March 2022. Publisher: Nature Publishing Group.

[3] Xiao Li and Hongwei Zhu. Two-dimensional MoS2: Properties, preparation, and applications. *Journal of Materiomics*, 1(1):33–44, March 2015.

[4] Sajedeh Manzeli, Dmitry Ovchinnikov, Diego Pasquier, Oleg V. Yazyev, and Andras Kis. 2D transition metal dichalcogenides. *Nature Reviews Materials*, 2(8):1–15, June 2017. Number: 8 Publisher: Nature Publishing Group.

[5] N. Divya Bharathi and K. Sivasankaran. Research progress and challenges of two dimensional MoS2 field effect transistors. *Journal of Semiconductors*, 39(10):104002, October 2018. Publisher: Chinese Institute of Electronics.

[6] Ribu Mathew and J. Ajayan. Material processing, performance and reliability of MoS2 field effect transistor (FET) technology- A critical review. *Materials Science in Semiconductor Processing*, 160:107397, June 2023.

[7] Xin Tong, Eric Ashalley, Feng Lin, Handong Li, and Zhiming M. Wang. Advances in MoS2-Based Field Effect Transistors (FETs). *Nano-Micro Letters*, 7(3):203–218, July 2015.

[8] Hari Singh Nalwa. A review of molybdenum disulfide (MoS 2) based photodetectors: from ultra-broadband, self-powered to flexible devices. *RSC Advances*, 10(51):30529–30602, 2020. Publisher: Royal Society of Chemistry.

[9] Riya Wadhwa, Abhay V. Agrawal, and Mukesh Kumar. A strategic review of recent progress, prospects and challenges of MoS2-based photodetectors. *Journal of Physics D: Applied Physics*, 55(6):063002, October 2021. Publisher: IOP Publishing.

[10] Alberto Taffelli, Sandra Dirè, Alberto Quaranta, and Lucio Pancheri. MoS2 Based Photodetectors: A Review. *Sensors (Basel, Switzerland)*, 21, April 2021.

[11] Jyah Strachan, Anthony F. Masters, and Thomas Maschmeyer. 3R-MoS2 in Review: History, Status, and Outlook. *ACS Applied Energy Materials*, 4(8):7405–7418, August 2021. Publisher: American Chemical Society.

[12] Roscoe G. Dickinson and Linus Pauling. THE CRYSTAL STRUCTURE OF MOLYBDENITE. *Journal of the American Chemical Society*, 45(6):1466–1471, June 1923. Publisher: American Chemical Society.

[13] R. F. Frindt, A. D. Yoffe, and Frank Philip Bowden. Physical properties of layer structures : optical properties and photoconductivity of thin crystals of molybdenum disulphide. *Proceedings of the Royal Society of London. Series A. Mathematical and Physical Sciences*, 273(1352):69–83, January 1997. Publisher: Royal Society.

[14] Per Joensen, R. F. Frindt, and S. Roy Morrison. Single-layer MoS2. *Materials Research Bulletin*, 21(4):457–461, April 1986.

[15] A. K. Geim and I. V. Grigorieva. Van der Waals heterostructures. *Nature*, 499(7459):419–425, July 2013. Number: 7459 Publisher: Nature Publishing Group.

[16] Kin Fai Mak and Jie Shan. Photonics and optoelectronics of 2D semiconductor transition metal dichalcogenides. *Nature Photonics*, 10(4):216–226, April 2016. Number: 4 Publisher: Nature Publishing Group.

[17] A. Chaves, J. G. Azadani, Hussain Alsalman, D. R. da Costa, R. Frisenda, A. J. Chaves, Seung Hyun Song, Y. D. Kim, Daowei He, Jiadong Zhou, A. Castellanos-Gomez, F. M. Peeters, Zheng Liu, C. L. Hinkle, Sang-Hyun Oh, Peide D. Ye, Steven J. Koester, Young Hee Lee, Ph Avouris, Xinran Wang, and Tony Low. Bandgap engineering of two-dimensional semiconductor materials. *npj 2D Materials and Applications*, 4(1):1–21, August 2020. Number: 1 Publisher: Nature Publishing Group.

[18] Deep Jariwala, Vinod K. Sangwan, Lincoln J. Lauhon, Tobin J. Marks, and Mark C. Hersam. Emerging Device Applications for Semiconducting Two-Dimensional Transition Metal Dichalcogenides. *ACS Nano*, 8(2):1102–1120, February 2014. Publisher: American Chemical Society.

[19] Ming-hong Wu, Lin Li, Ning Liu, De-jin Wang, Yuan-cheng Xue, and Liang Tang. Molybdenum disulfide (MoS2) as a co-catalyst for photocatalytic degradation of organic contaminants: A review. *Process Safety and Environmental Protection*, 118:40–58, August 2018.

[20] Andrea Splendiani, Liang Sun, Yuanbo Zhang, Tianshu Li, Jonghwan Kim, Chi-Yung Chim, Giulia Galli, and Feng Wang. Emerging Photoluminescence in Monolayer MoS2. *Nano Letters*, 10(4):1271–1275, April 2010. Publisher: American Chemical Society.

[21] Tawinan Cheiwchanchamnangij and Walter R. L. Lambrecht. Quasiparticle band structure calculation of monolayer, bilayer, and bulk MoS$\{\}_\{2\}$. *Physical Review B*, 85(20):205302, May 2012. Publisher: American Physical Society.

[22] S. Lebègue and O. Eriksson. Electronic structure of two-dimensional crystals from ab initio theory. *Physical Review B*, 79(11):115409, March 2009. Publisher: American Physical Society.

[23] Tianshu Li and Giulia Galli. Electronic Properties of MoS2 Nanoparticles. *The Journal of Physical Chemistry C*, 111(44):16192–16196, November 2007. Publisher: American Chemical Society.

[24] Eugene S. Kadantsev and Pawel Hawrylak. Electronic structure of a single MoS2 monolayer. *Solid State Communications*, 152(10):909–913, May 2012.

[25] A. Kuc, N. Zibouche, and T. Heine. Influence of quantum confinement on the electronic structure of the transition metal sulfide TS$\{\}_\{2\}$. *Physical Review B*, 83(24):245213, June 2011. Publisher: American Physical Society.

[26] Sarah L. Howell, Deep Jariwala, Chung-Chiang Wu, Kan-Sheng Chen, Vinod K. Sangwan, Junmo Kang, Tobin J. Marks, Mark C. Hersam, and Lincoln J. Lauhon. Investigation of Band-Offsets at Monolayer–Multilayer MoS2 Junctions by Scanning Photocurrent Microscopy. *Nano Letters*, 15(4):2278–2284, April 2015. Publisher: American Chemical Society.

[27] Jason K. Ellis, Melissa J. Lucero, and Gustavo E. Scuseria. The indirect to direct band gap transition in multilayered MoS2 as predicted by screened hybrid density functional theory. *Applied Physics Letters*, 99(26):261908, December 2011.

[28] Jian Wang, Shuyan Xu, Congcong Zhang, Ailing Yin, Mingyuan Sun, Hongru Yang, Chenguo Hu, and Hong Liu. Field effect transistor-based tactile sensors: From

sensor configurations to advanced applications. *InfoMat*, 5(1):e12376, 2023. _eprint: https://onlinelibrary.wiley.com/doi/pdf/10.1002/inf2.12376.

[29] Ertürk Enver Yildirim, Luis Antonio Panes-Ruiz, Pratyaksh Yemulwar, Ebru Cihan, Bergoi Ibarlucea, and Gianaurelio Cuniberti. Carbon nanotube neurotransistors with ambipolar memory and learning functions. *MRS Bulletin*, 48(12):1208–1220, December 2023.

[30] Basudev Nag Chowdhury and Sanatan Chattopadhyay. Dual-Gate GaAs-Nanowire FET for Room Temperature Charge-Qubit Operation: A NEGF Approach. *Advanced Quantum Technologies*, 6(4):2200072, 2023. _eprint: https://onlinelibrary.wiley.com/doi/pdf/10.1002/qute.202200072.

[31] R.-H. Yan, A. Ourmazd, and K.F. Lee. Scaling the Si MOSFET: from bulk to SOI to bulk. *IEEE Transactions on Electron Devices*, 39(7):1704–1710, July 1992. Conference Name: IEEE Transactions on Electron Devices.

[32] F. Schwierz, J. Pezoldt, and R. Granzner. Two-dimensional materials and their prospects in transistor electronics. *Nanoscale*, 7(18):8261–8283, 2015. Publisher: Royal Society of Chemistry.

[33] Muhammad Sanaullah and Masud H Chowdhury. Subthreshold swing characteristics of multilayer MoS2 tunnel FET. In *2015 IEEE 58th International Midwest Symposium on Circuits and Systems (MWSCAS)*, pages 1–4, August 2015. ISSN: 1558-3899.

[34] He Tian, Zhen Tan, Can Wu, Xiaomu Wang, Mohammad Ali Mohammad, Dan Xie, Yi Yang, Jing Wang, Lain-Jong Li, Jun Xu, and Tian-Ling Ren. Novel Field-Effect Schottky Barrier Transistors Based on Graphene-MoS2 Heterojunctions. *Scientific Reports*, 4(1):5951, August 2014. Number: 1 Publisher: Nature Publishing Group.

[35] Wenzhao Wang, Jichang Lu, Da Wan, Xiangbin Zeng, Jingjing Lu, Tingwei Xu, Chen Chen, and Tao Zhang. Improved performance in MoS2 homogeneous junction field effect transistors by optimizing electrodes contact. *Materials Science and Engineering: B*, 290:116348, April 2023.

[36] B. Radisavljevic, A. Radenovic, J. Brivio, V. Giacometti, and A. Kis. Single-layer MoS2 transistors. *Nature Nanotechnology*, 6(3):147–150, March 2011. Number: 3 Publisher: Nature Publishing Group.

[37] Gwan-Hyoung Lee, Young-Jun Yu, Xu Cui, Nicholas Petrone, Chul-Ho Lee, Min Sup Choi, Dae-Yeong Lee, Changgu Lee, Won Jong Yoo, Kenji Watanabe, Takashi Taniguchi, Colin Nuckolls, Philip Kim, and James Hone. Flexible and Transparent MoS2 Field-Effect Transistors on Hexagonal Boron Nitride-Graphene Heterostructures. *ACS Nano*, 7(9):7931–7936, September 2013. Publisher: American Chemical Society.

[38] Ah-Jin Cho, Suk Yang, Kyung Park, Seok Daniel Namgung, Hojoong Kim, and Jang-Yeon Kwon. Multi-Layer MoS2 FET with Small Hysteresis by Using Atomic Layer Deposition Al2O3 as Gate Insulator. *ECS Solid State Letters*, 3(10):Q67, August 2014. Publisher: IOP Publishing.

[39] Yan Chen, Xudong Wang, Peng Wang, Hai Huang, Guangjian Wu, Bobo Tian, Zhenchen Hong, Yutao Wang, Shuo Sun, Hong Shen, Jianlu Wang, Weida Hu, Jinglan Sun, Xiangjian Meng, and Junhao Chu. Optoelectronic Properties of Few-Layer MoS2 FET Gated by Ferroelectric Relaxor Polymer. *ACS Applied Materials & Interfaces*, 8(47):32083–32088, November 2016. Publisher: American Chemical Society.

[40] Jiyue Zou, Lisheng Wang, and Fengxiang Chen. Improved performance of top-gated multilayer MoS2 transistors with channel fully encapsulated by Al2O3 dielectric. *AIP Advances*, 9(9):095061, September 2019.

[41] Xiao Wang, Tian-Bao Zhang, Wen Yang, Hao Zhu, Lin Chen, Qing-Qing Sun, and David Wei Zhang. Improved integration of ultra-thin high-k dielectrics in few-layer MoS2 FET by remote forming gas plasma pretreatment. *Applied Physics Letters*, 110(5):053110, February 2017.

[42] Sudharsanam Subramaniyam, Sasikala Muthusamy, and Sudhakar K. Bharatan. Simulation of Molybdenum Disulfide based MOSFET Device using COMSOL Multiphysics software. *Journal of Physics: Conference Series*, 2312(1):012057, August 2022. Publisher: IOP Publishing.

[43] Agraj Khare and Priyanka Dwivedi. Design, simulation and optimization of multi-layered MoS2 based FET devices. *Engineering Research Express*, 3(4):045046, December 2021. Publisher: IOP Publishing.

[44] Nicola Pelagalli, Emiliano Laudadio, Pierluigi Stipa, Davide Mencarelli, and Luca Pierantoni. Efficient and Versatile Modeling of Mono- and Multi-Layer MoS2 Field

Effect Transistor. *Electronics*, 9(9):1385, September 2020. Number: 9 Publisher: Multidisciplinary Digital Publishing Institute.

[45] Sreevatsan Radhakrishnan, Suggula Naga Sai Vishnu, Syed Ishtiyaq Ahmed, and Rajagopalan Thiruvengadathan. Effects of Channel Length Scaling on the Electrical Characteristics of Multilayer MoS2 Field Effect Transistor. *Micromachines*, 14(2):275, February 2023. Number: 2 Publisher: Multidisciplinary Digital Publishing Institute.

[46] Ming Zhang, Po-Yen Chien, and Jason C. S. Woo. Comparative simulation study on MoS2 FET and CMOS transistor. In *2015 IEEE SOI-3D-Subthreshold Microelectronics Technology Unified Conference (S3S)*, pages 1–2, October 2015.

[47] N. Divya Bharathi and K. Sivasankaran. Influence of metal contact on the performance enhancement of monolayer MoS2 transistor. *Superlattices and Microstructures*, 120:479–486, August 2018.

[48] Gyuchull Han and Youngki Yoon. Contact-dependent performance variability of monolayer MoS2 field-effect transistors. *Applied Physics Letters*, 105(21):213508, November 2014.

[49] Baolin Wei and Chao Lu. Transition metal dichalcogenide MoS2 field-effect transistors for analog circuits: A simulation study. *AEU - International Journal of Electronics and Communications*, 88:110–119, May 2018.

[50] Marco Bernardi, Maurizia Palummo, and Jeffrey C. Grossman. Extraordinary sunlight absorption and one nanometer thick photovoltaics using two-dimensional monolayer materials. *Nano Letters*, 13(8):3664–3670, August 2013.

[51] Wei-Chu Shen, Ruei-San Chen, and Ying-Sheng Huang. Photoconductivities in MoS2 Nanoflake Photoconductors. *Nanoscale Research Letters*, 11(1):124, March 2016.

[52] Oriol Lopez-Sanchez, Dominik Lembke, Metin Kayci, Aleksandra Radenovic, and Andras Kis. Ultrasensitive photodetectors based on monolayer MoS2. *Nature Nanotechnology*, 8(7):497–501, July 2013. Publisher: Nature Publishing Group.

[53] Rui Cheng, Dehui Li, Hailong Zhou, Chen Wang, Anxiang Yin, Shan Jiang, Yuan Liu, Yu Chen, Yu Huang, and Xiangfeng Duan. Electroluminescence and Photocurrent Generation from Atomically Sharp WSe2/MoS2 Heterojunction p–n Diodes. *Nano Letters*, 14(10):5590–5597, October 2014. Publisher: American Chemical Society.

[54] Yan Chen, Xudong Wang, Guangjian Wu, Zhen Wang, Hehai Fang, Tie Lin, Shuo Sun, Hong Shen, Weida Hu, Jianlu Wang, Jinglan Sun, Xiangjian Meng, and Junhao Chu. High-Performance Photovoltaic Detector Based on MoTe2/MoS2 Van der Waals Heterostructure. *Small*, 14(9):1703293, 2018. _eprint: https://onlinelibrary.wiley.com/doi/pdf/10.1002/smll.201703293.

[55] Caihong Li, Juntong Zhu, Wen Du, Yixuan Huang, Hao Xu, Zhengang Zhai, and Guifu Zou. The Photodetectors Based on Lateral Monolayer MoS2/WS2 Heterojunctions. *Nanoscale Research Letters*, 16(1):123, July 2021.

[56] L. Britnell, R. M. Ribeiro, A. Eckmann, R. Jalil, B. D. Belle, A. Mishchenko, Y.-J. Kim, R. V. Gorbachev, T. Georgiou, S. V. Morozov, A. N. Grigorenko, A. K. Geim, C. Casiraghi, A. H. Castro Neto, and K. S. Novoselov. Strong light-matter interactions in heterostructures of atomically thin films. *Science (New York, N.Y.)*, 340(6138):1311–1314, June 2013.

[57] Hao Gu, Shan-Ci Chen, and Qingdong Zheng. Emerging Perovskite Materials with Different Nanostructures for Photodetectors. *Advanced Optical Materials*, 9(5):2001637, 2021. _eprint: https://onlinelibrary.wiley.com/doi/pdf/10.1002/adom.202001637.

[58] Xiaochi Liu, Min Sup Choi, Euyheon Hwang, Won Jong Yoo, and Jian Sun. Fermi Level Pinning Dependent 2D Semiconductor Devices: Challenges and Prospects. *Advanced Materials (Deerfield Beach, Fla.)*, 34(15):e2108425, April 2022.

[59] Changsik Kim, Inyong Moon, Daeyeong Lee, Min Sup Choi, Faisal Ahmed, Seunggeol Nam, Yeonchoo Cho, Hyeon-Jin Shin, Seongjun Park, and Won Jong Yoo. Fermi Level Pinning at Electrical Metal Contacts of Monolayer Molybdenum Dichalcogenides. *ACS nano*, 11(2):1588–1596, February 2017.

[60] Alessandro Grillo and Antonio Di Bartolomeo. A Current–Voltage Model for Double Schottky Barrier Devices. *Advanced Electronic Materials*, 7(2):2000979, February 2021.

[61] Youngsin Park, Nannan Li, Daesung Jung, Laishram Tomba Singh, Jaeyoon Baik, Eunsook Lee, Dongseok Oh, Young Dok Kim, Jin Yong Lee, Jeongseok Woo, Seungmin Park, Hanchul Kim, Geunseop Lee, Geunsik Lee, and Chan-Cuk Hwang. Unveiling the origin of n-type doping of natural MoS2: carbon. *npj 2D Materials and Applications*, 7(1):1–7, September 2023. Number: 1 Publisher: Nature Publishing Group.

[62] Kapildeb Dolui, Ivan Rungger, and Stefano Sanvito. Origin of the n-type and p-type conductivity of MoS${}_{2}$ monolayers on a SiO${}_{2}$ substrate. *Physical Review B*, 87(16):165402, April 2013. Publisher: American Physical Society.

[63] Saptarshi Das, Abhijith Prakash, Ramon Salazar, and Joerg Appenzeller. Toward Low-Power Electronics: Tunneling Phenomena in Transition Metal Dichalcogenides. *ACS Nano*, 8(2):1681–1689, February 2014. Publisher: American Chemical Society.

[64] Naveen Kaushik, Ankur Nipane, Firdous Basheer, Sudipta Dubey, Sameer Grover, Mandar M. Deshmukh, and Saurabh Lodha. Schottky barrier heights for Au and Pd contacts to MoS2. *Applied Physics Letters*, 105(11):113505, September 2014.

[65] Yan Wang, Jong Chan Kim, Yang Li, Kyung Yeol Ma, Seokmo Hong, Minsu Kim, Hyeon Suk Shin, Hu Young Jeong, and Manish Chhowalla. P-type electrical contacts for 2D transition-metal dichalcogenides. *Nature*, 610(7930):61–66, October 2022. Number: 7930 Publisher: Nature Publishing Group.

[66] Saptarshi Das, Hong-Yan Chen, Ashish Verma Penumatcha, and Joerg Appenzeller. High performance multilayer MoS2 transistors with scandium contacts. *Nano Letters*, 13(1):100–105, January 2013.

[67] Zhongjun Li, Xingxing Li, and Jinlong Yang. Comparative Study on Electronic Structures of Sc and Ti Contacts with Monolayer and Multilayer MoS2. *ACS Applied Materials & Interfaces*, 7(23):12981–12987, June 2015. Publisher: American Chemical Society.

[68] Kraig Andrews, Arthur Bowman, Upendra Rijal, Pai-Yen Chen, and Zhixian Zhou. Improved Contacts and Device Performance in MoS2 Transistors Using a 2D Semiconductor Interlayer. *ACS Nano*, 14(5):6232–6241, May 2020. Publisher: American Chemical Society.

[69] Timothy N. Walter, Kayla A. Cooley, Anna C. Domask, and Suzanne E. Mohney. Nickel diffusion into MoS2 and the effect of annealing on contact resistance. *Materials Science in Semiconductor Processing*, 107:104850, March 2020.

[70] Dongwon Choi, Jeehoon Jeon, Tae-Eon Park, Byeong-Kwon Ju, and Ki-Young Lee. Schottky barrier height engineering on MoS2 field-effect transistors using a polymer surface modifier on a contact electrode. *Discover Nano*, 18(1):80, May 2023.

[71] Marcio Fontana, Tristan Deppe, Anthony K. Boyd, Mohamed Rinzan, Amy Y. Liu, Makarand Paranjape, and Paola Barbara. Electron-hole transport and photovoltaic

effect in gated MoS2 Schottky junctions. *Scientific Reports*, 3(1):1634, April 2013. Number: 1 Publisher: Nature Publishing Group.

[72] W. Van Roosbroeck. Theory of the flow of electrons and holes in germanium and other semiconductors. *The Bell System Technical Journal*, 29(4):560–607, October 1950. Conference Name: The Bell System Technical Journal.

[73] Abhijith Prakash, Hesameddin Ilatikhameneh, Peng Wu, and Joerg Appenzeller. Understanding contact gating in Schottky barrier transistors from 2D channels. *Scientific Reports*, 7(1):12596, October 2017. Number: 1 Publisher: Nature Publishing Group.

[74] D.J. Frank, Y. Taur, and H.-S.P. Wong. Generalized scale length for two-dimensional effects in MOSFETs. *IEEE Electron Device Letters*, 19(10):385–387, October 1998.

[75] Qian Xie, Chen Chen, Mingjun Liu, Shuang Xia, and Zheng Wang. Short-channel effects on the static noise margin of 6T SRAM composed of 2D semiconductor MOSFETs. *Science China Information Sciences*, 62(6):62404, January 2019.

[76] Transition Metal Dichalcogenide Schottky Barrier Transistors: A Device Analysis and Material Comparison. In Alessandro Michel Houssa Molle, Athanasios Dimoulas, editor, *2D Materials for Nanoelectronics*. CRC Press, 2016. Num Pages: 34.

[77] James Nagel and Nageljr@ieee Org. Solving the Generalized Poisson Equation Using the Finite-Difference Method (FDM). February 2011.

[78] Stephen D. Gedney. *Introduction to the Finite-Difference Time-Domain (FDTD) Method for Electromagnetics*. Morgan & Claypool Publishers, 2011. Google-Books-ID: sdwbsMAztKIC.

[79] T.C. Banwell and A. Jayakumar. Exact analytical solution for current flow through diode with series resistance. *Electronics Letters*, 36(4):291, 2000.

[80] Kane Yee. Numerical solution of initial boundary value problems involving maxwell's equations in isotropic media. *IEEE Transactions on Antennas and Propagation*, 14(3):302–307, May 1966. Conference Name: IEEE Transactions on Antennas and Propagation.

[81] Kin Fai Mak, Changgu Lee, James Hone, Jie Shan, and Tony F. Heinz. Atomically thin MoS: a new direct-gap semiconductor. *Physical Review Letters*, 105(13):136805, September 2010.

[82] J. Appenzeller, M. Radosavljević, J. Knoch, and Ph. Avouris. Tunneling Versus Thermionic Emission in One-Dimensional Semiconductors. *Physical Review Letters*, 92(4):048301, January 2004.

[83] Ana Conde-Rubio, Xia Liu, Giovanni Boero, and Jürgen Brugger. Edge-Contact MoS2 Transistors Fabricated Using Thermal Scanning Probe Lithography. *ACS Applied Materials & Interfaces*, 14(37):42328–42336, September 2022.

[84] Penglu Yang, Sneha Banerjee, Wenjun Kuang, Yu Ding, Quan Ma, and Peng Zhang. Current crowding and spreading resistance of electrical contacts with irregular contact edges. *Journal of Physics D: Applied Physics*, 53(48):485303, November 2020.

[85] Min Sup Choi, Nasir Ali, Tien Dat Ngo, Hyungyu Choi, Byungdu Oh, Heejun Yang, and Won Jong Yoo. Recent Progress in 1D Contacts for 2D-Material-Based Devices. *Advanced Materials*, 34(39):2202408, 2022. _eprint: https://onlinelibrary.wiley.com/doi/pdf/10.1002/adma.202202408.

[86] Yi Ren, Xiaoyang Yang, Li Zhou, Jing-Yu Mao, Su-Ting Han, and Ye Zhou. Recent Advances in Ambipolar Transistors for Functional Applications. *Advanced Functional Materials*, 29(40):1902105, 2019. _eprint: https://onlinelibrary.wiley.com/doi/pdf/10.1002/adfm.201902105.

[87] Siqi Hu, Jinpeng Xu, Qinghua Zhao, Xiaoguang Luo, Xutao Zhang, Tao Wang, Wanqi Jie, Yingchun Cheng, Riccardo Frisenda, Andres Castellanos-Gomez, and Xuetao Gan. Gate-Switchable Photovoltaic Effect in BP/MoTe2 van der Waals Heterojunctions for Self-Driven Logic Optoelectronics. *Advanced Optical Materials*, 9(5):2001802, 2021. _eprint: https://onlinelibrary.wiley.com/doi/pdf/10.1002/adom.202001802.

[88] Yuchen Du, Han Liu, Yexin Deng, and Peide D. Ye. Device Perspective for Black Phosphorus Field-Effect Transistors: Contact Resistance, Ambipolar Behavior, and Scaling. *ACS Nano*, 8(10):10035–10042, October 2014. Publisher: American Chemical Society.

[89] Mikai Chen, Hongsuk Nam, Sungjin Wi, Lian Ji, Xin Ren, Lifeng Bian, Shulong Lu, and Xiaogan Liang. Stable few-layer MoS2 rectifying diodes formed by plasma-assisted doping. *Applied Physics Letters*, 103(14):142110, October 2013.

[90] Y. J. Zhang, J. T. Ye, Y. Yomogida, T. Takenobu, and Y. Iwasa. Formation of a Stable p–n Junction in a Liquid-Gated MoS2 Ambipolar Transistor. *Nano Letters*, 13(7):3023–3028, July 2013. Publisher: American Chemical Society.

[91] Surajit Sutar, Pratik Agnihotri, Everett Comfort, T. Taniguchi, K. Watanabe, and Ji Ung Lee. Reconfigurable p-n junction diodes and the photovoltaic effect in exfoliated MoS2 films. *Applied Physics Letters*, 104(12):122104, March 2014.

[92] Britton W. H. Baugher, Hugh O. H. Churchill, Yafang Yang, and Pablo Jarillo-Herrero. Optoelectronic devices based on electrically tunable p–n diodes in a monolayer dichalcogenide. *Nature Nanotechnology*, 9(4):262–267, April 2014. Publisher: Nature Publishing Group.

[93] J. Lee, P. Gipp, and C. Heller. Carbon nanotube p-n junction diodes. *Applied Physics Letters*, 85:145–147, July 2004.

[94] Wenwen Fei, Jens Trommer, Max Christian Lemme, Thomas Mikolajick, and André Heinzig. Emerging reconfigurable electronic devices based on two-dimensional materials: A review. *InfoMat*, 4(10):e12355, 2022. _eprint: https://onlinelibrary.wiley.com/doi/pdf/10.1002/inf2.12355.

[95] Yue Pang, Yaoqiang Zhou, Lei Tong, and Jianbin Xu. 2D Dual Gate Field-Effect Transistor Enabled Versatile Functions. *Small*, n/a(n/a):2304173. _eprint: https://onlinelibrary.wiley.com/doi/pdf/10.1002/smll.202304173.

[96] Gilles Buchs, Maria Barkelid, Salvatore Bagiante, Gary A. Steele, and Val Zwiller. Imaging the formation of a p-n junction in a suspended carbon nanotube with scanning photocurrent microscopy. *Journal of Applied Physics*, 110(7):074308, October 2011.

[97] Saptarshi Das and Joerg Appenzeller. WSe2 field effect transistors with enhanced ambipolar characteristics. *Applied Physics Letters*, 103(10), September 2013. Publisher: AIP Publishing.

[98] V. Sverdlov, E. Ungersboeck, H. Kosina, and S. Selberherr. Current transport models for nanoscale semiconductor devices. *Materials Science and Engineering: R: Reports*, 58(6):228–270, January 2008.

[99] Van-Nam Do. Non-equilibrium Green function method: theory and application in simulation of nanometer electronic devices. *Advances in Natural Sciences: Nanoscience and Nanotechnology*, 5(3):033001, June 2014. Publisher: IOP Publishing.